Mon. Not. R. Astron. Soc. 000, 1–28 (1997) Printed 26 May 1997 (MN LATEX style file v1.4)

An H I Aperture Synthesis Mosaic of the Small Magellanic Cloud

L. Staveley-Smith,[1⋆] R.J. Sault,[1] D. Hatzidimitriou,[2] M.J. Kesteven[1] and D. McConnell[1]

[1] *Australia Telescope National Facility, CSIRO, P.O. Box 76, Epping, NSW 2121, Australia*
[2] *Physics Department, University of Crete, 714.09 Heraklion, Crete, Greece*

Accepted 1996 September 16. Received 1996 September 9; in original form 1996 July 23

ABSTRACT

We present the results of a survey of neutral hydrogen emission in the Small Magellanic Cloud (SMC) with the Australia Telescope Compact Array (ATCA). The survey consists of a mosaic of 320 separate pointings of the 375-m array, resulting in a resolution of 1.6 arcmin (28 pc, for a distance of 60 kpc) over a field of 20 deg^2. The rms brightness temperature sensitivity is 1.4 K, corresponding to an H I column-density sensitivity of 4×10^{18} cm^{-2} for each velocity channel of width 1.6 km s^{-1}. The H I distribution is complex and, on scales $\lesssim$ 1 kpc, appears to be dominated by the effects of expanding H I shells, which are probably driven by the combined effects of supernovae and stellar winds from massive stars. The picture of the SMC that arises from the current data seems to challenge the earlier belief that the SMC consists of two or more spatially separate structures with different systemic velocities. We find that the observed multiple components are, in many cases, caused by the combined effects of the numerous shells and supershells. Altogether, we identify six supershells (defined here as those with radii greater than 300 pc) and 495 giant shells. For each of these, we measure positions, radii, velocities and expansion rates, and derive ages and kinetic energy requirements. The apparent age distribution of shells is remarkably narrow, with a mean age of 5.4 Myr and an intrinsic dispersion of 2 Myr. Southern shells appear to be older, on average, by 2.5 Myr. The kinetic energy of the shells is a large fraction of the gravitational binding energy of the SMC, implying that further disintegration of the SMC will occur with time, and especially at the next close passage with the LMC or the Galaxy, unless the SMC possesses a massive halo. Because of their interferometric nature, the images presented here are insensitive to structures of size $\gtrsim 0\overset{\circ}{.}6$, and should not be used for deriving *total* H I column densities.

Key words: galaxies: galaxies: kinematics and dynamics – Magellanic Clouds – radio lines: ISM – ISM: atoms – kinematics and dynamics – surveys.

1 INTRODUCTION

The SMC is the nearest gas-rich galaxy to our Galaxy, and remains amongst the lowest metallicity galaxies known. It has experienced a different evolutionary history from that of our Galaxy, and it appears to have had a recent encounter with its close companion, the Large Magellanic Cloud (LMC) (Murai & Fujimoto 1980; Gardiner, Sawa & Fujimoto 1994) towards which there is a gaseous (McGee & Newton 1981) and stellar (Irwin 1991) bridge. As a low-mass, dwarf, irregular galaxy in an interacting system of galaxies, the SMC is able to promote our understanding of the evolution of such galaxies, and the relative roles of internal and external perturbations in stimulating star formation. The detailed study of the gaseous content of the SMC, in particular, can provide us with insights into the condensation of molecular clouds, the formation of globular clusters, the effect of early star-formation on the interstellar medium, and the subsequent triggering of secondary star-formation through interstellar shocks.

A drawback in detailed studies of the SMC has been the relatively poor spatial resolution (260 pc)[†] of existing maps of H I in the SMC, resulting from the limited resolution of

⋆ E-mail: lstavele@atnf.csiro.au

† We assume a distance to the SMC of 60 kpc throughout this paper

the Parkes telescope at λ21 cm. These studies include those published by Hindman (1967), McGee & Newton (1981) and Mathewson, Ford & Visvanathan (1988). Hindman interpreted the SMC as an edge-on rotating disk, but drew attention to the importance of expanding shells of gas. McGee & Newton focused more on the apparent sub-structure of the SMC, as did Mathewson et al. who also obtained Cepheid distances which indicate a significant line-of-sight depth to the SMC. Higher spatial resolutions are provided by Hα Fabry-Perot studies (Torres & Carranza 1987), though these have a more patchy velocity field. By comparison with the Parkes data, *IRAS* far infrared maps (Schwering & Israel 1990) are able to probe dust clouds of size $\lesssim$ 100 pc, studies of molecular clouds at millimetre wavelengths are able to attain resolutions $\lesssim$ 13 pc (Rubio et al. 1993), and detailed optical studies are able to probe scales $\lesssim$ 1 pc. Moreover, by analogy with the Galaxy, we can expect considerable structure in the neutral interstellar medium (ISM) down to scales of $\sim$ 10 pc (Crovisier & Dickey 1983).

The ATCA is reconfigurable and offers a range of resolutions. We chose to survey the SMC with the relatively compact 375-m array. This gives an angular resolution of 1.6 arcmin (28 pc), while at the same time giving good surface-brightness sensitivity such that the whole of the SMC can be surveyed in a moderate amount of observing time. A few preliminary results from this survey have been presented elsewhere (Staveley-Smith et al. 1995), though the reduction strategy used here supersedes that work.

In this paper, we describe the observing strategy in Section 2. The data reduction, which involves mosaicing many fields together, is described in Section 3. The data are presented in the form of images in Section 4, and the catalogue of shells and supershells is presented and discussed in Section 5. In Section 6, we include a discussion of the structure and evolution of the SMC, and in Section 7 we re-discuss the depth of the SMC. Future papers will present column-density measurements, large-scale kinematics, radio-continuum observations, and comparisons with other wavebands.

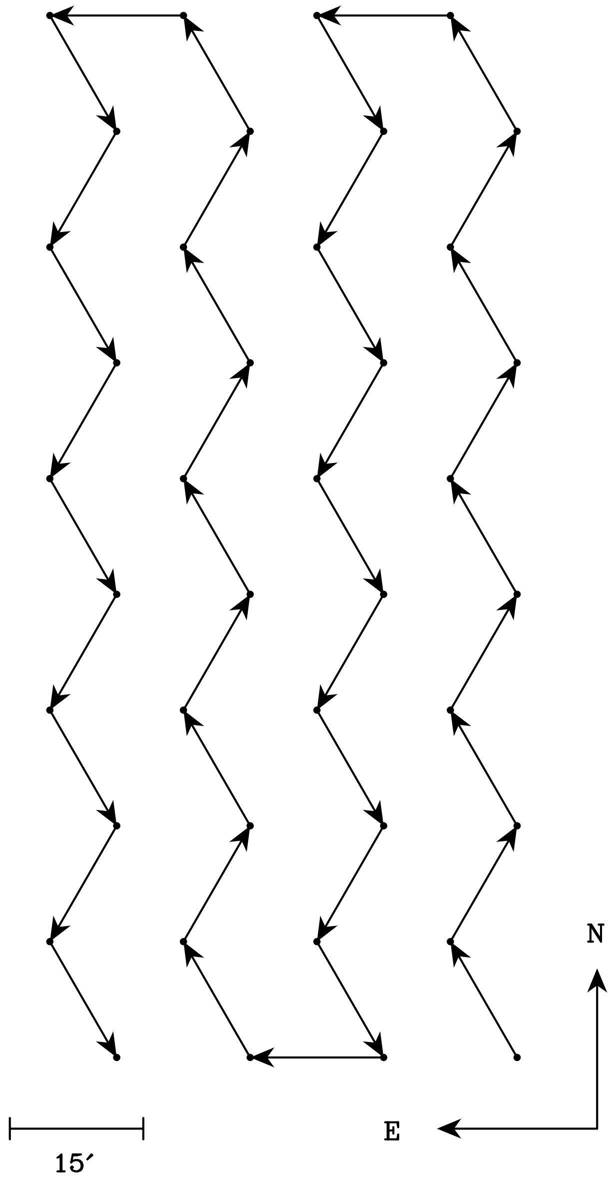

Figure 1. The SMC was surveyed in eight segments of 40 fields using a 'point-and-shoot' technique. The basic pattern for each of these segments is shown. To minimize drive time (a total time of 20 s per field, including antenna drive, was permitted), the telescopes were made to execute the raster pattern shown.

2 OBSERVATIONS

The observations were taken over eight days from 1992 October 6 to 1992 October 14 (October 8 was lost because of high wind). The 375-m configuration of the ATCA was used. This configuration has 10 baselines which are all even multiples (2, 4, 6, 8, 12, 14, 16, 18, 22 and 30) of the basic ATCA 15.3-m increment. The central observing frequency was 1420 MHz. The bandwidth of 4 MHz (844 km s^{-1}) was divided into 1024 channels, resulting in a channel spacing of 0.82 km s^{-1}. During data reduction, the data were boxcar-averaged into 78 $\times$ 1.6 km s^{-1} channels, covering a heliocentric velocity range from 88 to 216 km s^{-1}, and resulting in a FWHP velocity resolution of 1.54 km s^{-1}. For presentation purposes only (Section 4), the data were further boxcar-averaged into 40 $\times$ 3.3 km s^{-1} channels. The mean system temperature during the observations was 40 K.

On each of the observing days, the array was cycled around 40 adjacent fields in a raster pattern, as shown in Fig. 1. Each field was observed for 16.1 s, and the array was moved to the next field (allowing 3.9 s for the antenna drive), thus executing a complete cycle in 800 s. After every third cycle, the secondary calibrator, PKS B0252–712, was observed for $\sim$ 100 s. During a typical day's observation of 12 – 14 h, each individual field was visited $\sim$ 50 times, resulting in a typical integration time of $\sim$ 800 s per field. The fields were placed on a hexagonal grid of side 15 arcmin. This gives considerable overlap between fields (the FWHP antenna primary beamwidth is 34 arcmin), and allows the recovery of some the 'missing' radial spacings in the *uv*-plane (Cornwell 1988; Cornwell, Holdaway & Uson 1993). The resultant coverage of the *uv*-plane for each of the eight observing days is shown in Fig. 2.

The total area covered is $4^{\circ}\!.5 \times 4^{\circ}\!.5$ centred on RA $01^{\rm h}01^{\rm m}$, Dec $-72^{\circ}56'$ (J2000). This area was chosen from existing single-dish maps (Hindman 1967; McGee & New-

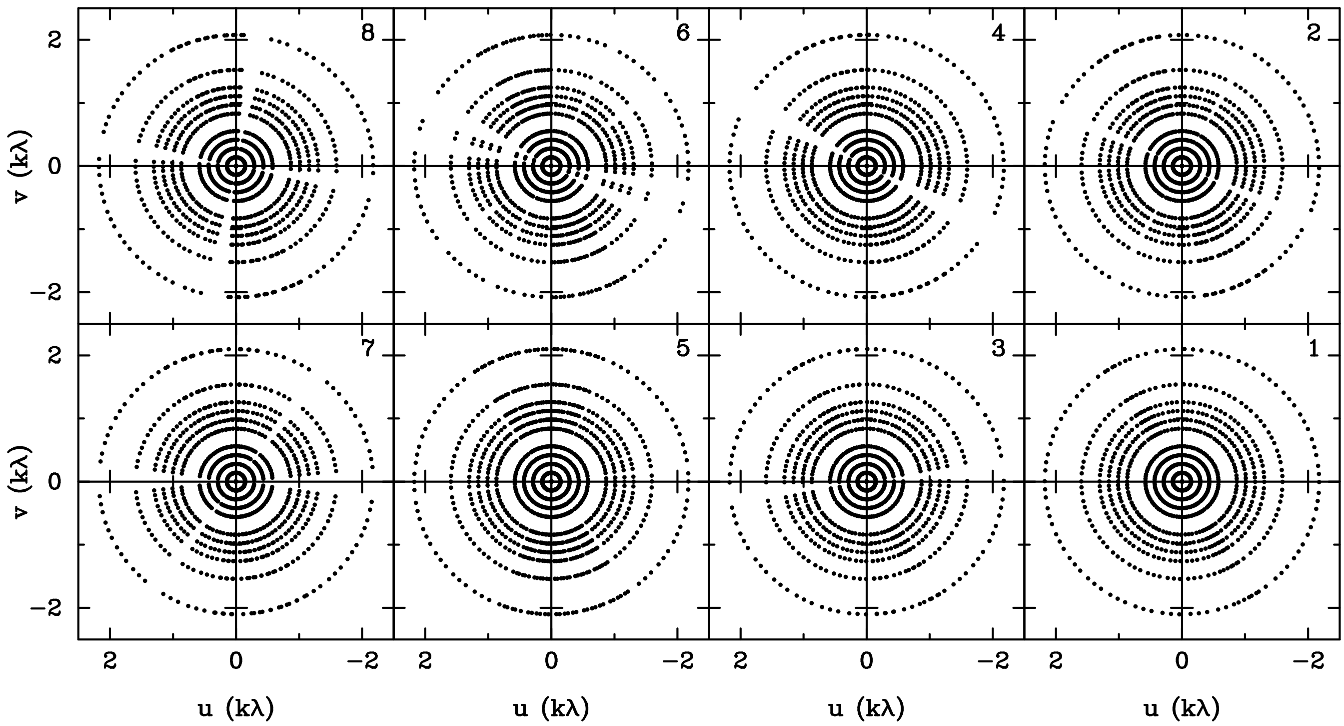

Figure 2. The coverage in the uv-plane of the observations of the SMC for each of the eight observing days. The coverage is only plotted for the 20th field observed on a particular day (i.e. fields 20, 60, 100, 140, 180, 220, 260 and 300, corresponding to days 1-8 respectively). The day number at the top right of each sub-plot corresponds to the observing day (1992 October 6,7 or 9–14 respectively). The actual uv-coverage is greatly improved after mosaicing, because of the influence of neighbouring fields.

ton 1981) to encompass the main body of H I in the SMC above a column density of 10^{21} cm^{-2} (7.5 M$_\odot$ pc^{-2}) and extends well outside the optical bar of the SMC. The distribution of the field centres is shown in Fig. 3, superimposed on an Hα image provided by S.Kim and M.Bessell (private communication). The distribution of fields is based on a tangent point of RA $00^{\rm h}55^{\rm m}$, Dec $-72°50'$ (J2000), a point close to the centre of the optical bar.

Daily observations of PKS B1934–638 were made to define the absolute flux density scale and for bandpass calibration purposes.

3 DATA REDUCTION

3.1 Editing and Calibration

Initial reductions were done in AIPS. Data taken when the telescope was off-source were flagged (these data were identified by an on-line monitoring program). For calibration purposes only, the data were then averaged in frequency and a small amount of further flagging was done. Amplitude and phase calibration was done using 0252–712 which was estimated to have a flux density of 5.48 ± 0.01 Jy relative to the known flux density for 1934–638 of 14.9 Jy at 1.42 GHz. Calibration only modified the complex gain of the antennas by a few per cent over the course of each day because of the stability of the observing conditions and instrument. The revised complex antenna gains were applied to the SMC spectral-line data using two-point interpolation from the calibrator data. Bandpass calibration, using 1934–638, was applied, the data from each linear polarization were averaged together to form Stokes I, and the data were continuum-subtracted in the uv-plane with the AIPS task UVLSF. The continuum channels were chosen to avoid the range of emission present in the Galaxy and the SMC, and lie in three ranges: −89 to −32 km s^{-1}, 51 to 92 km s^{-1} and 207 to 306 km s^{-1}. It will be noted in the final images that there is some residual emission above 207 km s^{-1}, i.e. within the velocity range assumed to be line-free. This leads to a small underestimation of flux densities in the north-east of the SMC. This is the reason for four small 'shadows' centred near RA $01^{\rm h}15^{\rm m}$, Dec $-72°$ (J2000) which can be seen by carefully inspecting the low-velocity images. Heliocentric corrections, accurate to < 0.1 km s^{-1}, were applied to the data with the AIPS task CVEL. We used a heliocentric 'radio' velocity convention ($v = c\Delta\nu/\nu_\circ$), which agrees with the normal 'optical' convention ($v = c\Delta\lambda/\lambda_\circ$) to better than 0.2 km s^{-1} over the entire SMC velocity range.

3.2 Mosaicing

To create an image of the entire SMC, the data for the individual fields need to be mosaiced. Cornwell (1988) describes the theory of mosaicing aperture synthesis data in a manner which uses all the information present, and allows for the recovery of 'missing' spacings in the uv-plane (see also Ekers & Rots 1979). As noted by Cornwell, this allows us to retain spatial information on angular scales up to about $\lambda/(B_{\rm min} - D/2) = 0\overset{\circ}{.}6$, where the minimum baseline $B_{\rm min} = 30.6$ m, the antenna diameter $D = 22$ m, and the wavelength $\lambda = 0.211$ m.

The SMC data were mosaiced in the MIRIAD system

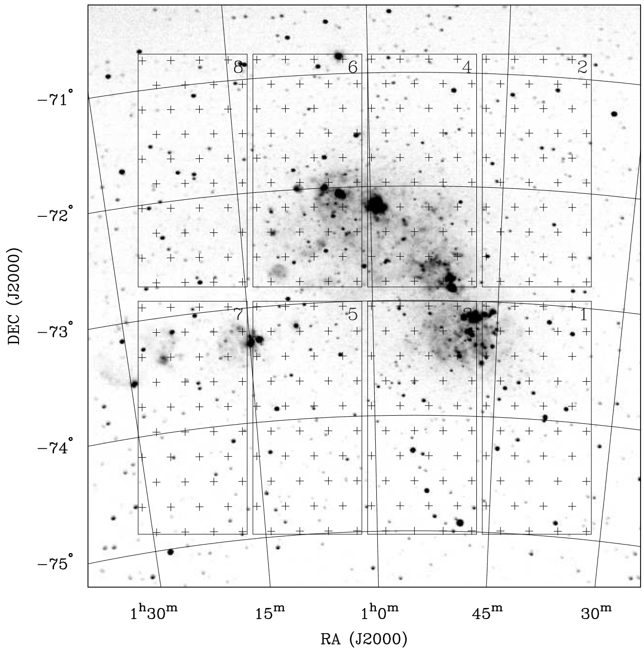

Figure 3. The distribution of the observed fields (+) on the sky, superimposed on an Hα image taken at Siding Spring Observatory by S. Kim and M. Bessell (private communication). The boxes enclose fields observed during the same day (as in Fig.2).

(Sault, Teuben & Wright 1995) using a new suite of software the workings of which are described in more detail by Sault, Staveley-Smith & Brouw (1996). The INVERT task was used to make a so-called 'linear mosaic' from the *uv*-data from the 320 SMC fields. To do this, the data for each velocity channel were Fourier transformed into the image plane using a projection with a common tangent point at RA $00^{\rm h}55^{\rm m}$, Dec $-72°50'$ (J2000). The details of this projection are given in Appendix A. 'Uniform' weighting was applied to the *uv*-data before transformation although, because of the large sub-image size used, this is almost equivalent to 'natural' weighting (Sault et al. 1996). The sub-image size for each field is 115×115 pixels each of size 30 arcsec, and is phase-shifted such that the sub-image centre is always an integral number of pixels from the tangent point in each dimension. The large sub-image size of 57.5×57.5 arcmin is required to cover the ATCA FWHP primary beam (FWHP 34 arcmin at 1.42 GHz). It also covers the $\lambda/30.6$-m and $\lambda/15.3$-m grating rings at radii 23.7 and 47.4 arcmin, respectively. These sub-images were combined to form a 'dirty' mosaiced image using a weight proportional to the primary beam response at a given position. Because of the east-west nature of the ATCA, the output map is geometrically exact (Sault et al. 1996). This process was repeated for each of the 78 velocity channels of interest to form a cube of size $578 \times 610 \times 78$ in RA, Dec and velocity, respectively.

The 'dirty' cube was then spatially deconvolved (task MOSMEM) using the set of 320 point-spread functions (PSFs) created by the INVERT task. At each position in the dirty cube, the appropriate PSF is a linear combination of the individual PSFs (weight proportional to the primary beam response). The deconvolution procedure takes into account this spatial variance in the PSF. It also recovers all the extra *uv* information made available by sampling the sky at the Nyquist rate, as do more conventional 'joint' deconvolution procedures (Cornwell et al. 1993) which mosaic the sub-images during the deconvolution stage. However, the method we use (as detailed in Sault et al. 1996) has large practical advantages because of the smaller book-keeping and disk-space requirements. The deconvolution was done using a maximum-entropy algorithm. As with other deconvolution procedures, this algorithm will attempt to extrapolate to angular scales beyond those measured by the interferometer. We particularly note that any power present in our images with a spatial wavelength greater than $0\overset{\circ}{.}6$ is not reliably imaged, and that there is a non-zero and position-dependent 'DC offset' which will bias column density measurements. Finally, the maximum-entropy model was convolved with a circular Gaussian of FWHP 98 arcsec, and the image residuals added back in.

The final rms noise, measured in line-free parts of the final cube, is 22 mJy beam^{-1} compared with a theoretical noise estimate (based on a mean system temperature, and the theoretical antenna and correlator efficiencies) of 17 mJy beam^{-1} for the mosaiced data set. The corresponding $1-\sigma$ brightness temperature sensitivity is 1.4 K, or a column density sensitivity of 4.2×10^{18} cm^{-2} per 1.65 km s^{-1} channel.

Our mosaicing procedure deliberately does not completely correct for primary beam attenuation at the edge of the mosaic (see Fig. 3). This suppresses noise amplification which would otherwise artificially dominate the intensity range of the mosaic. Although this choice is largely one of presentation of the final images, there are advantages for some deconvolution processes in this approach (see Sault et al. 1996).

Note that the preliminary images presented by Staveley-Smith et al. (1995) were not made using the method described above. They are not geometrically exact in that there is a small rotational misalignment for each sub-field. They were also made using a conventional 'joint' deconvolution procedure.

4 IMAGES

Fig. 4 is a two-dimensional projection of the data cube which shows, for each position, the peak value of the brightness temperature at any velocity. The images for the individual velocity planes are shown in Fig. 5. For presentation purposes only, adjacent planes are averaged, resulting in 40 velocity planes with a spacing between planes of 3.3 km s^{-1} and the heliocentric velocity range (given in the top-left of each panel) of 89 to 215 km s^{-1}. For both figures, the greyscale range is -0.18 to 1.38 Jy beam^{-1}, corresponding to a brightness-temperature range of -11 to 87 K. The maximum brightness temperature is 126 K at RA $00^{\rm h}48^{\rm m}56^{\rm s}$, Dec $-73°03'38''$ (J2000). A J2000 coordinate grid is overlayed on each image. Because of the interferometric nature of the images in Figs 4 and 5, structure of size $\gtrsim 0\overset{\circ}{.}6$ is filtered out. Therefore these images are most useful for dynamical and morphological studies, and should not be used for purposes in which large-scale H I structure may play an important role (e.g. photoelectric absorption of background X-ray flux). We estimate that peak brightness temperatures are underestimated by about 40 per cent as a result of the

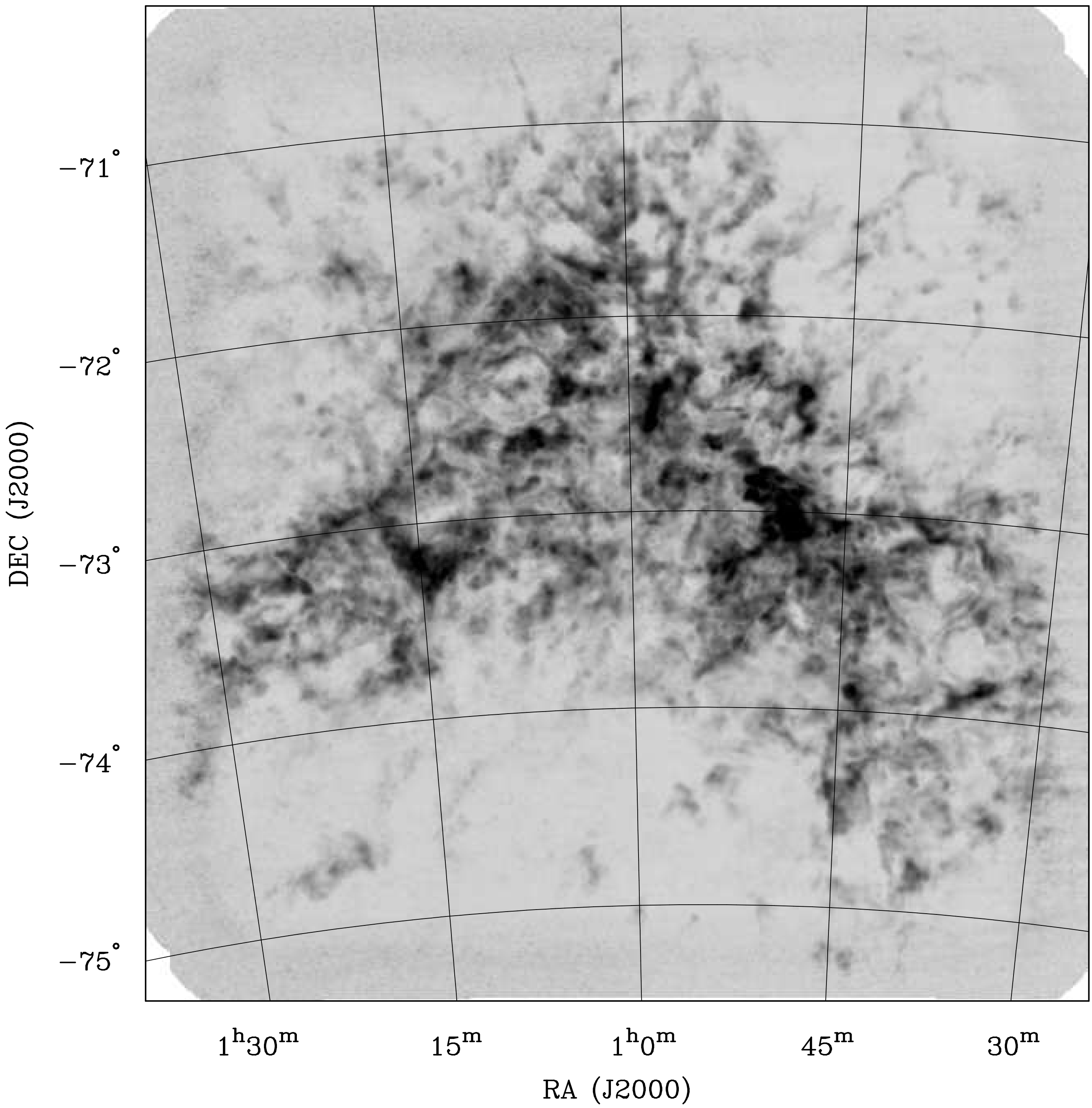

Figure 4. A mosaiced image of the SMC showing the peak brightness temperature as a function of position. A J2000 coordinate grid is overlayed. The grey-scale intensity range is −11 to 87 K with a linear transfer function. The maximum brightness temperature is 126 K.

lack of short spacings. H I masses of regions of size $\gtrsim 0\overset{\circ}{.}6$ are more severely affected, probably by a factor of between 2 – 4, depending on how the local DC offset is dealt with in the restored maximum entropy images. Observations which will lead to images sensitive to all spatial scales are under way, and will be reported in a future paper.

The overall area covered by the mosaic includes the region of the optically identified features of the 'Bar', 'Bright Arms', the 'Outer Arm' and 'Inner Wing' (Brück 1980). The iso-velocity images (Fig. 5) reveal a wealth of detailed structure seen for the first time in H I maps of the SMC. The complex structure is characterized by the presence of shells, arcs, filaments and knots. A detailed study of the shells follows in the next section. Visualized in the three dimensions of RA, Dec and velocity, the SMC has a distinctly frothy and filamentary appearance. The H I layer (Fig. 4) appears to be punctured by many holes and gives the impression of a disrupting system.

The progressive increase of (heliocentric) velocity of the H I from the south-west end of the bar to the north and east,

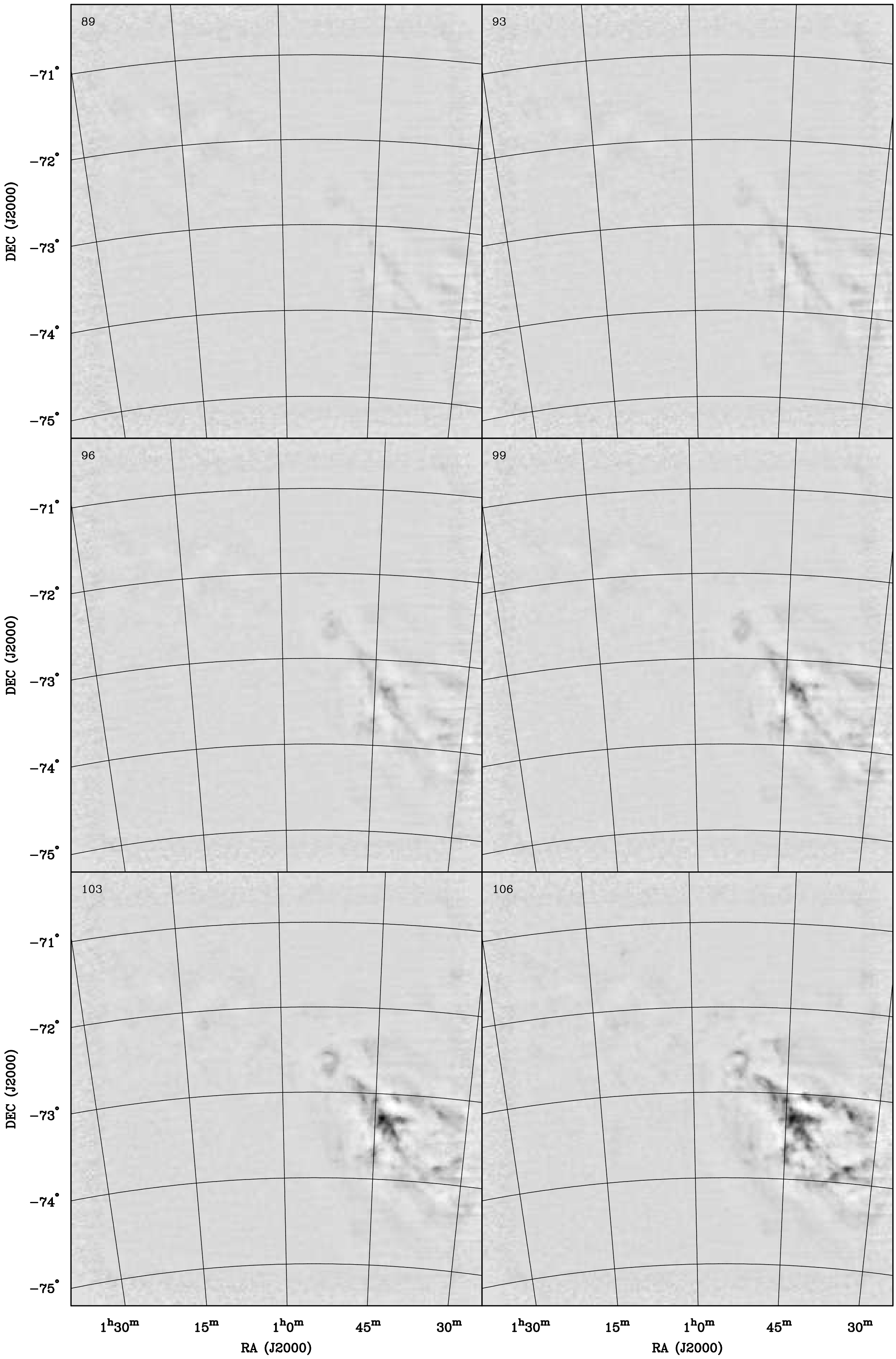

Figure 5. The H I mosaic of the SMC for 40 velocity planes between 89 and 215 km s^{-1} (heliocentric). Each panel is an RA–Dec image for the given heliocentric velocity which appears at the top-left. Each plane is 3.3 km s^{-1} wide and is an average of two planes in the processed cube. A J2000 coordinate grid is overlayed. The grey-scale intensity range is −11 to 87 K with a linear transfer function.

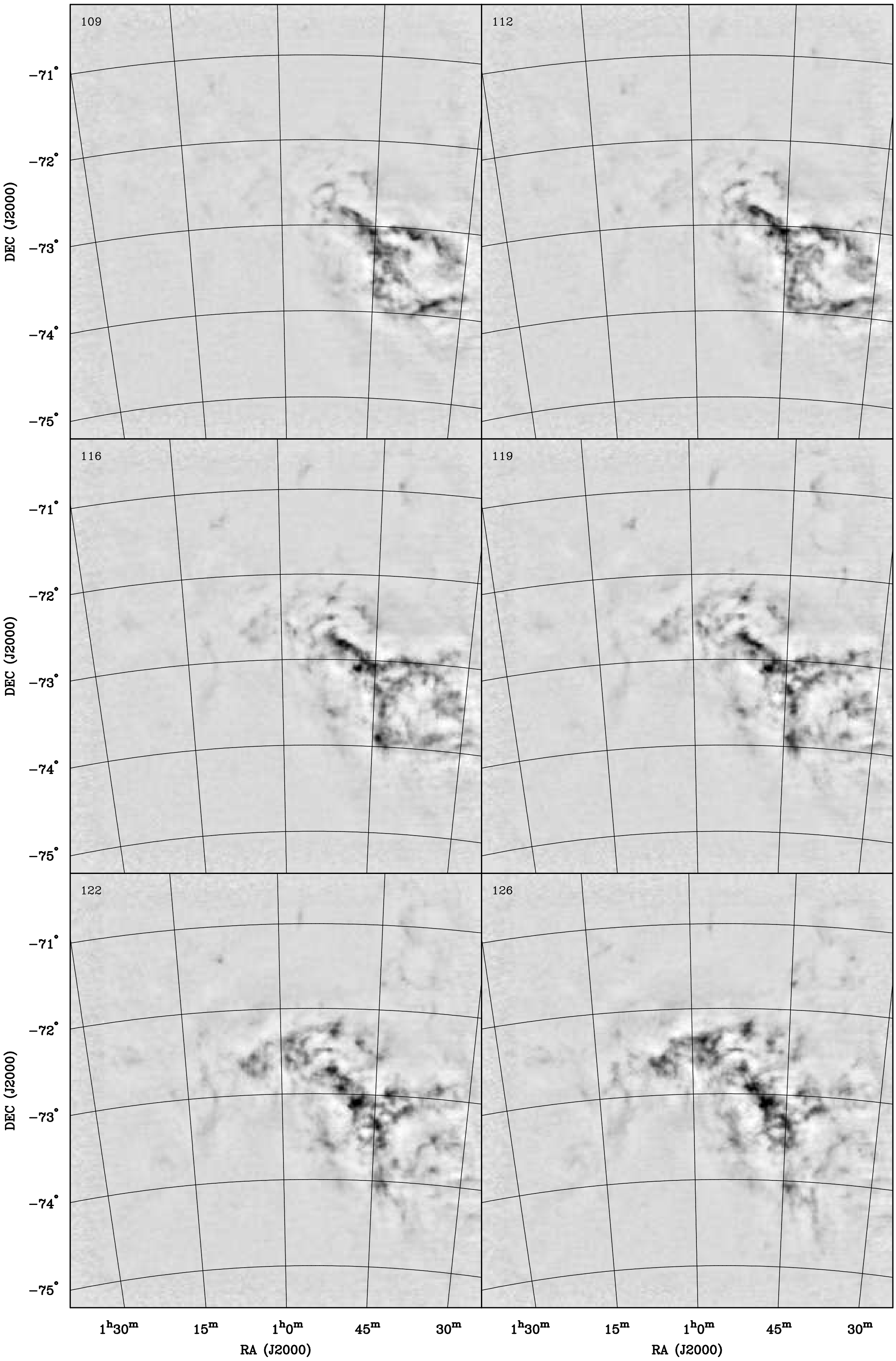

Figure 5 – *continued*

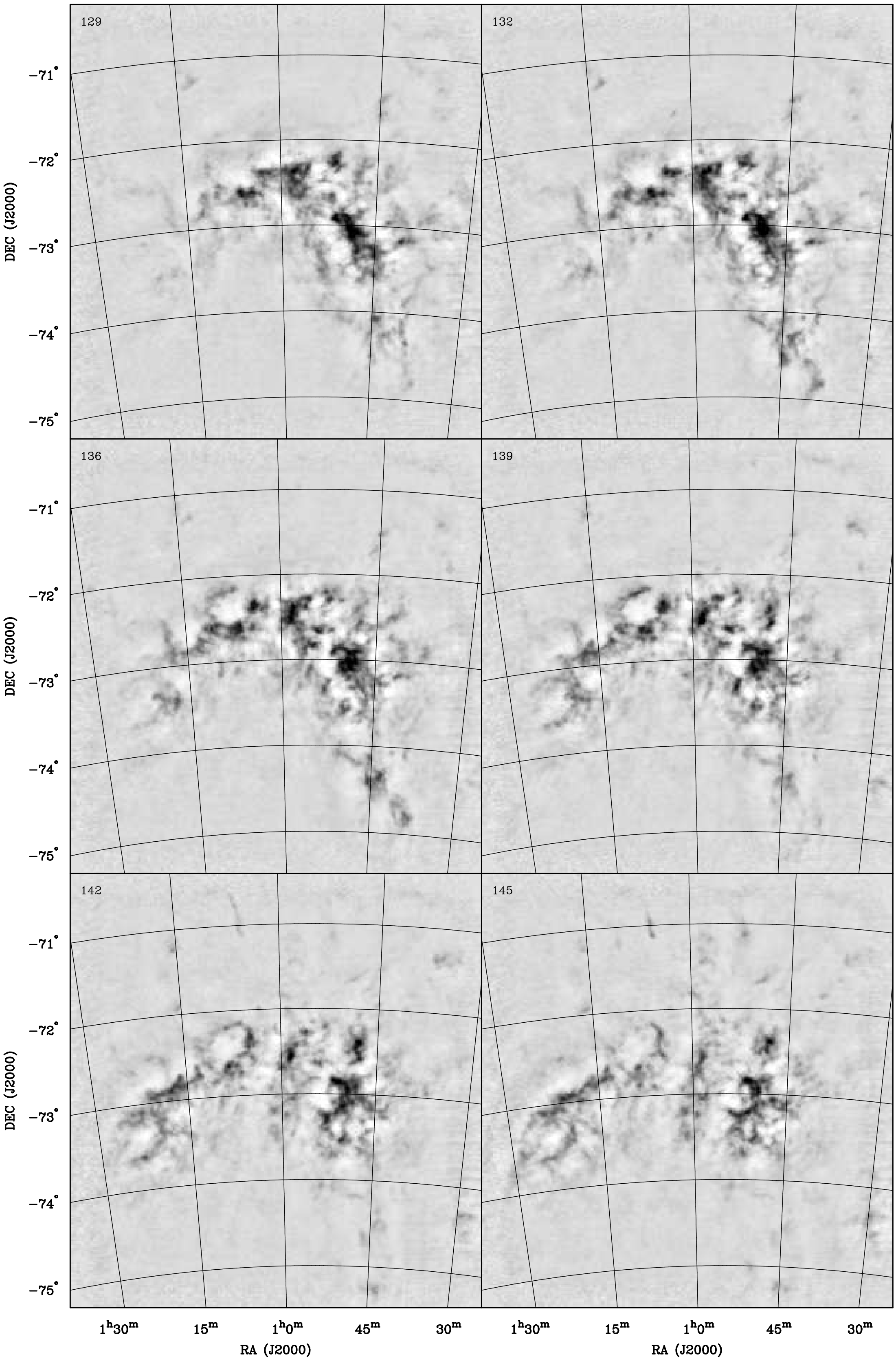

Figure 5 – *continued*

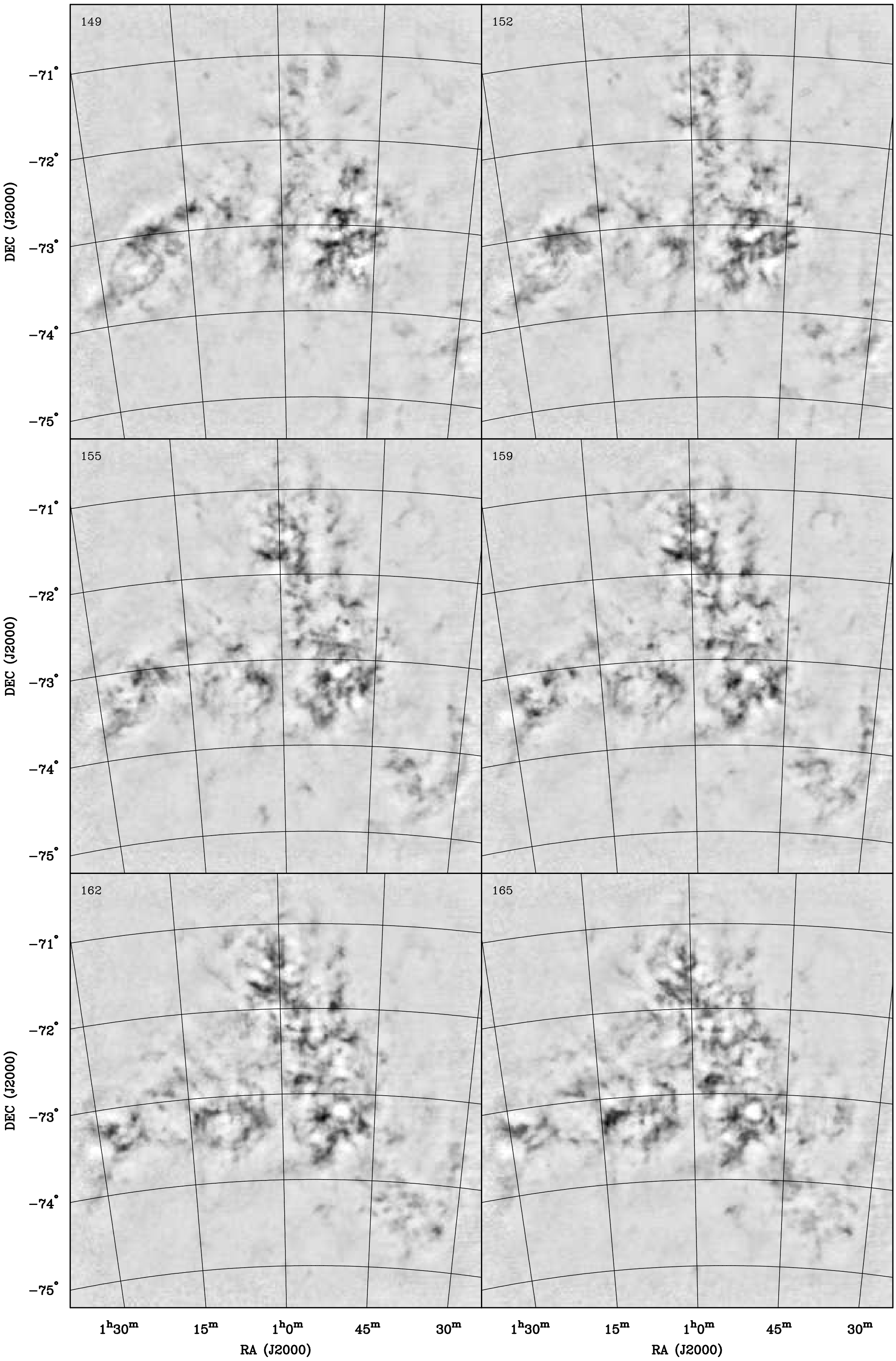

Figure 5 – *continued*

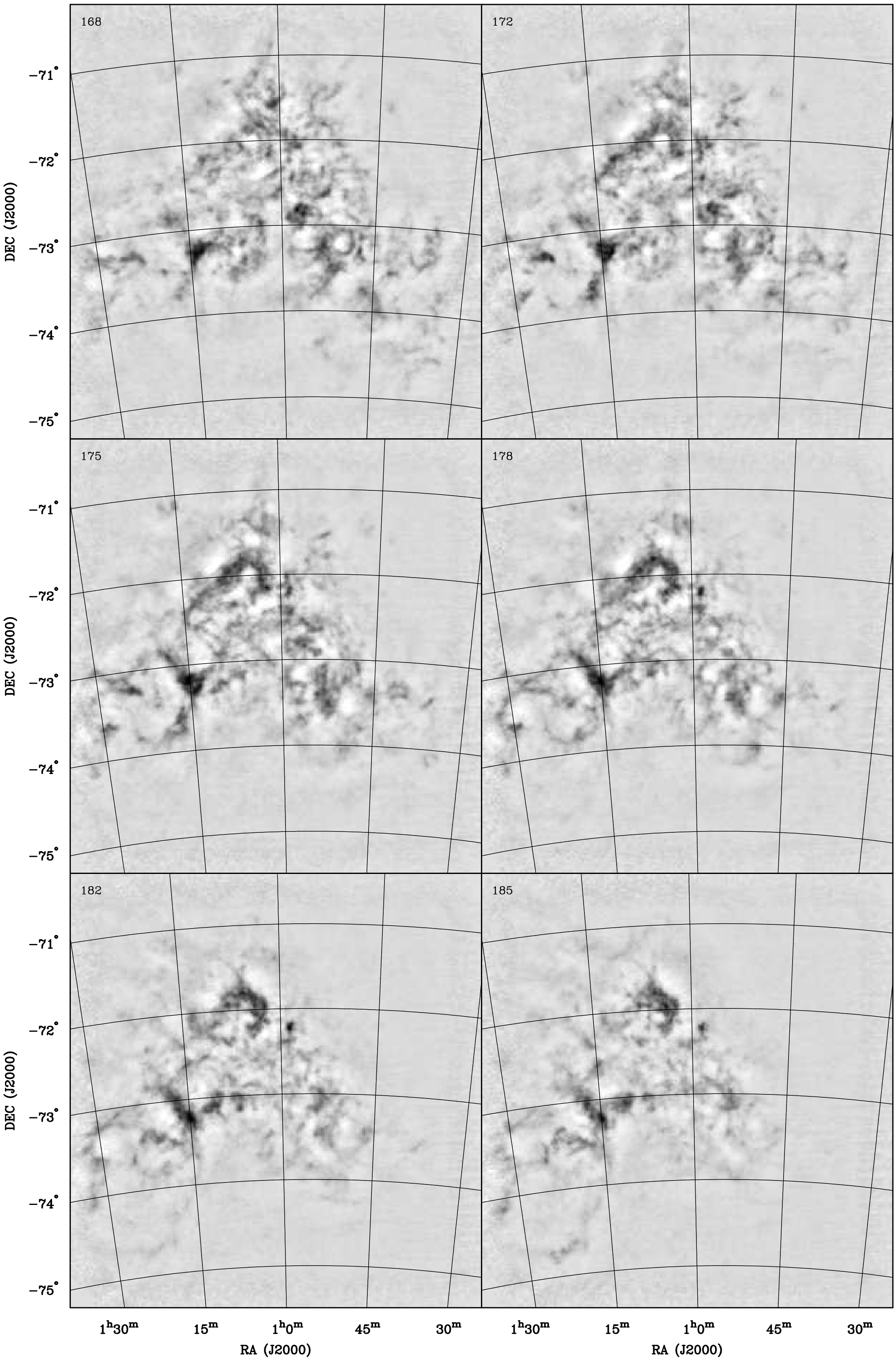

Figure 5 – *continued*

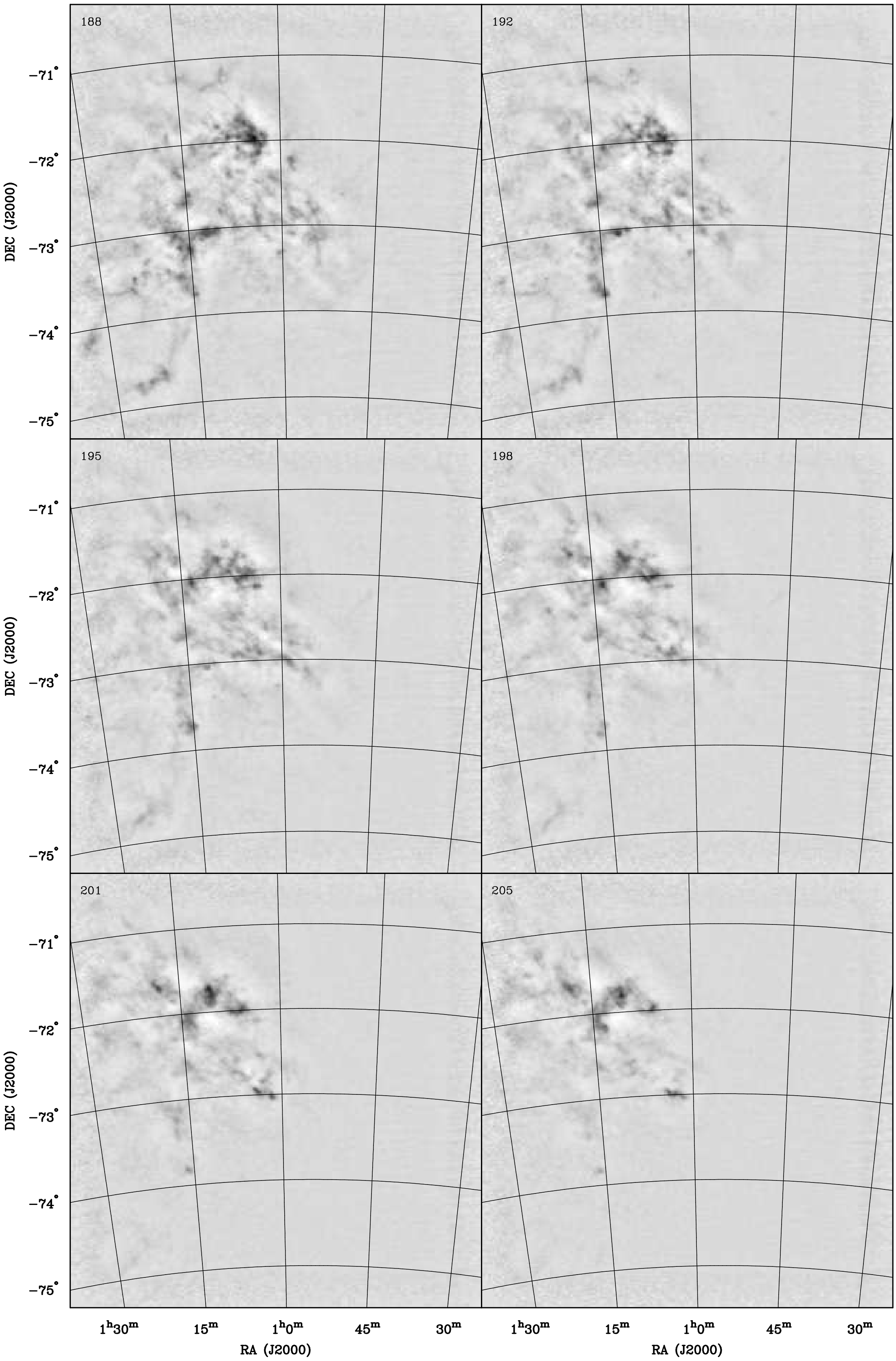

Figure 5 – *continued*

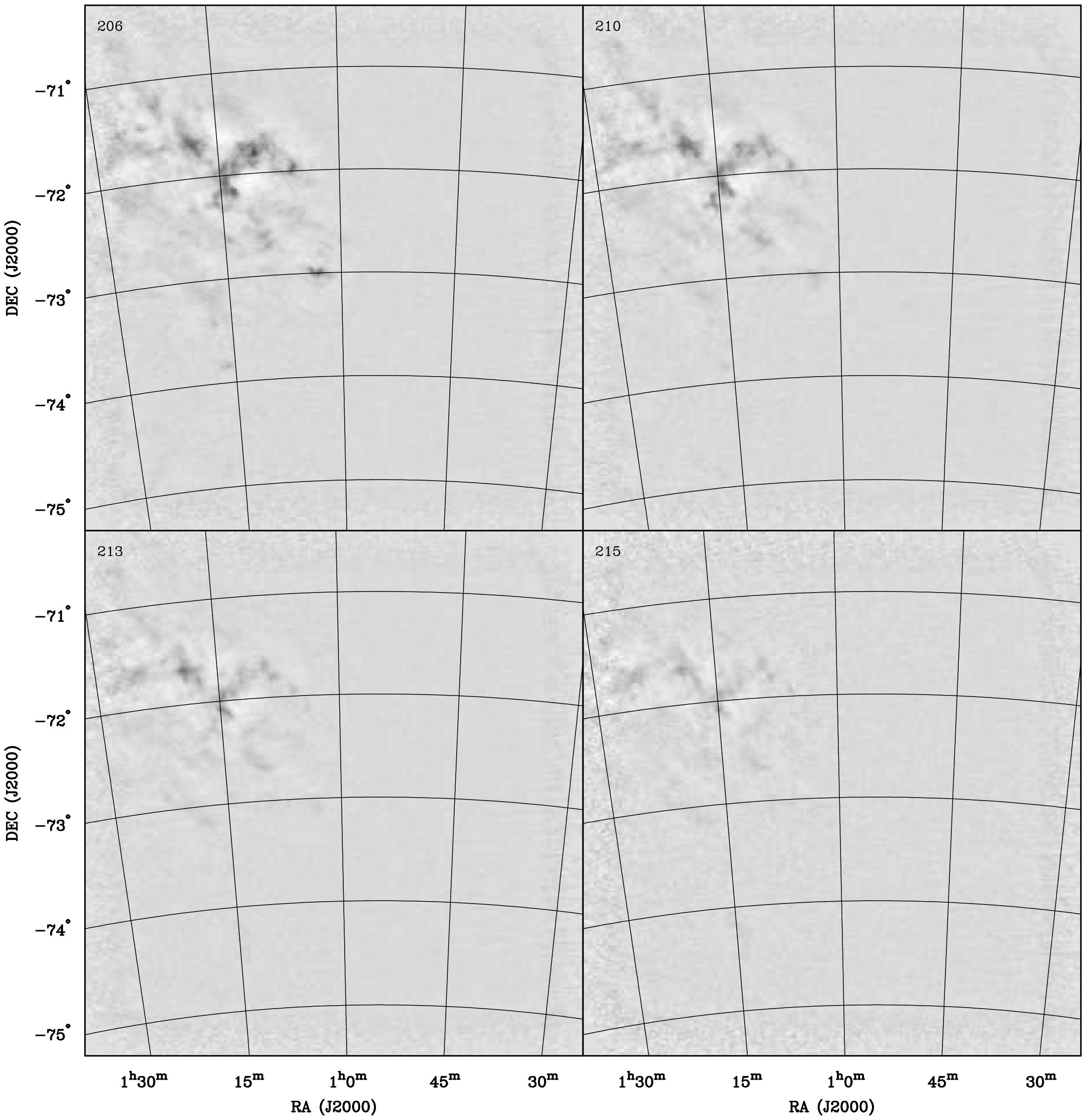

Figure 5 – *continued*

as seen in earlier studies (e.g. McGee & Newton 1981), is apparent. However, the overall H I appearance looks markedly different from earlier studies, because of the large amount of small-scale structure which occurs within the main confines of the SMC, and because of the population of surrounding clouds which are apparent in Fig. 5 above about a velocity of 114 km s^{-1} (Staveley-Smith et al. 1995).

5 SHELLS

Inspection of position-velocity images reveal many edge-brightened circular or elliptical structures, which are most easily explained as expanding shells of gas. Many similar structures are apparent in the Galaxy (Heiles 1979) and other galaxies (e.g. M31: Brinks & Bajaja 1986). Such structures appear to be driven by the mechanical energy input of the stellar winds from massive stars and supernovae which sweep up surrounding interstellar gas, although other mechanisms such as collisions between HVCs and galaxy disks have been postulated to explain the largest shells (Tenorio-Tagle & Bodenheimer 1988). Such structures are not unexpected in the SMC, given the low age of the stellar population and the high neutral gas fraction. Hindman (1967) identified three large shells from early Parkes observations, but many more have been identified in other low-luminosity gas-rich galaxies (e.g. Ho II, Puche et al. 1992; IC 2574, Martimbeau, Carignan & Roy 1994; NGC 1313, Ryder et al. 1995). Goudis & Meaburn (1978) and Meaburn (1980) were able to identify optically one candidate supergiant shell in the SMC, and 9 supergiant and 85 giant shells in the LMC. Detailed observations of some LMC shells, or superbubbles, have been made by Chu et al. (1995).

We have catalogued 501 expanding shells in the SMC. Most (343) were recognized and measured from their elliptical appearance on position-velocity images. The remainder (158) were initially identified from RA-Dec images, and then confirmed and measured on position-velocity images. Cross-checks were made to eliminate duplicate shells. The

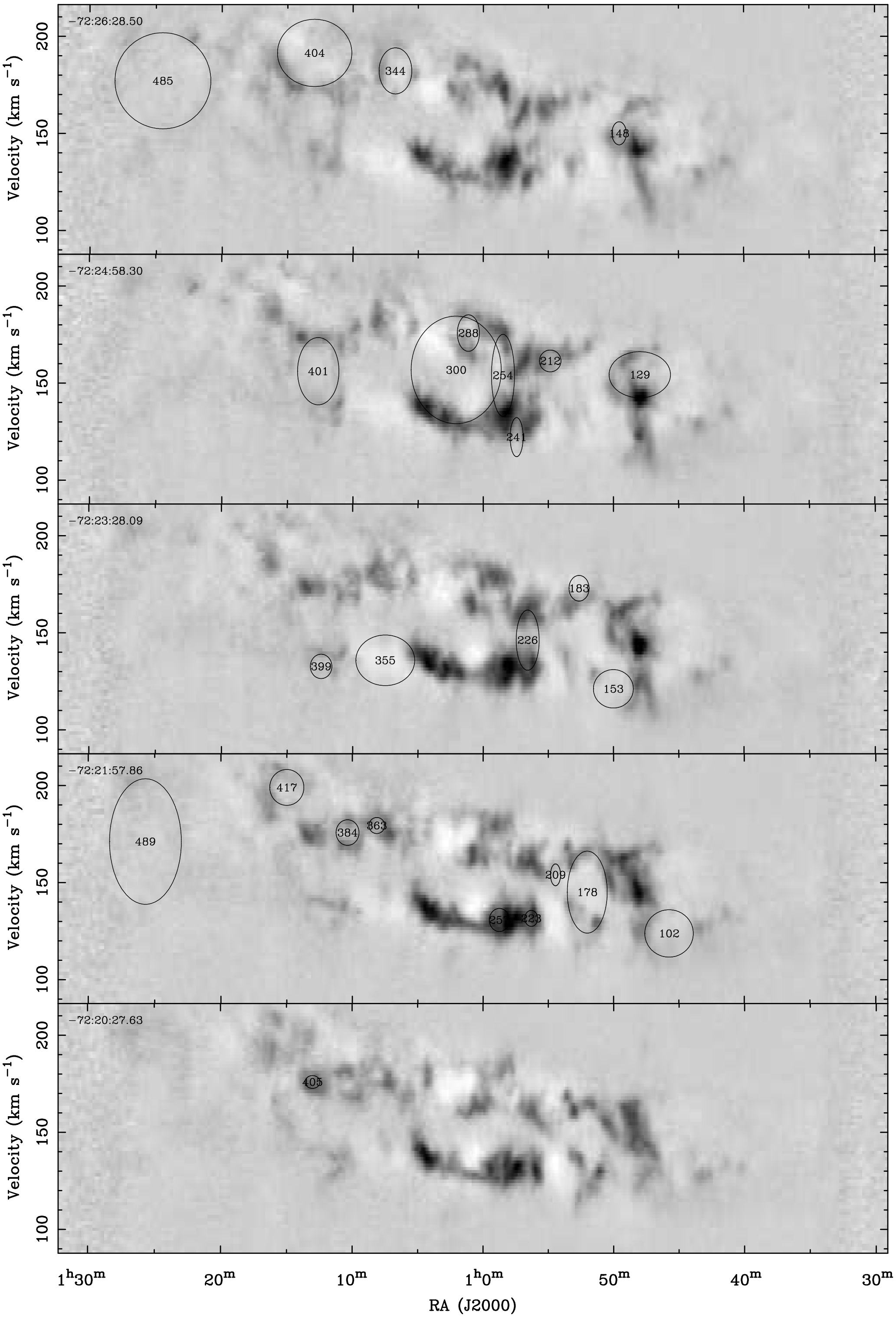

Figure 6. Five neighbouring RA-velocity images of the SMC near $\delta = -72°24'$ (J2000). Each image is a slice at constant y (see Appendix A). The central slice is at $y = 0°.44$, and the slices are separated by 1.5 arcmin. The approximate declination for each slice is given at the top left of each panel (the declinations are only exact at $\alpha = 00^h55^m$). The 26 shells which lie within the declination range plotted are overlayed as ellipses. The grey-scale range is -17 to 87 K (linear transfer function), with the peak interferometric brightness temperature being 112 K in this region. Several uncatalogued shell-like features can be seen. The appearance of the SMC in this region is dominated by SMC HI-300. Several of the smaller shells seem to occur on the rims of larger shells. Possible secondary shells of SMC HI-300 are SMC HI-288 and 344, both of which have ages consistent with this hypothesis. SMC HI-485 and 489 in the east are diffuse shells which are barely visible in these slices alone.

RA axis (or more strictly, the x-axis in Figs 3, 4 & 5, as defined in Appendix A) was used to represent position in the position-velocity images. Dimensions are measured in this plane only (thus ignoring ellipticity). An example of a sequence of position-velocity images is shown in Fig. 6, which also illustrates the appearance of expanding shells in this space. Several shells are present in these images, which represent only 5 of 216 such images examined. Ellipses, the dimensions of which represent the size and expansion velocity of all shells catalogued in these images, are overlayed.

Expansion velocities for a further 50 shells/holes identified in the RA-Dec images could not be measured, and are not catalogued. Many of these may be stationary, or very slow shells, although some of them may be artefacts caused by the complex structure of the SMC and the lack of short (zero) interferometer spacings.

For each of the total of 501 shells, we measured a position, a radius r_s, a central heliocentric velocity V, and an expansion velocity v_s (half the velocity separation of the peaks). These are listed in Table 1 together with estimates of age and mechanical wind luminosity. The errors in V and v_s are approximately $0.15v_s$, with a minimum error of 1 km s^{-1}. The error in r_s is approximately $0.15r_s$, with a minimum error of 1 arcmin (17 pc). The dynamical ages T_s, are calculated from $T_s = {}^3/_5(r_s/v_s)$ (Weaver et al. 1977), which assumes that, at the current stage of evolution, the mechanical energy providing the expansion of the shells has come from the continuous action of stellar winds from massive stars. The wind luminosity L_s is calculated from:

$$L_s = 1.5 \times 10^5 \left(\frac{r_s}{100 \text{ pc}}\right)^5 \left(\frac{T_s}{10^6 \text{ yr}}\right)^{-3} \left(\frac{n_\circ}{1 \text{ cm}^{-3}}\right) L_\odot \quad (1)$$

(from equation 21 of Weaver et al. 1977). The age and wind luminosity estimates are valid where the ambient density ($n_\circ$) is constant, the shells have not fragmented, the radiation pressure contribution is negligible, the stellar wind luminosity is constant, and the energy from supernovae is not yet significant (Tenorio-Tagle & Bodenheimer 1988). For most of the shells, which have $T_s < 10^7$ yr, the latter approximation is valid as stars with mass $< 20M_\odot$ are still on the main sequence. Older shells with $L_s > 200L_\odot$ (i.e. where an O star is likely to have been present), will have a significant supernova contribution. There are 15 such shells listed in Table 1 (assuming $n_\circ = 1$ cm^{-3}). The subsequent effect of supernova explosions has been discussed by McCray & Kafatos (1987). If the clusters are sufficiently large, the supernova energy deposition can be regarded as constant, and the shells will evolve in the same similar power-law fashion, with an average power still given by equation (1). Smaller clusters may be more easily re-accelerated by single supernova events, possibly leading to the dynamical discrepancies noted by Oey (1996) for some LMC superbubbles. However, equation (1) only applies before the shell reaches the 'snow-plough' phase, or until the shell breaks out of the galaxy, when the interior pressure will no longer be significant. Shull & Saken (1995) have used more realistic stellar wind models to investigate the influence of time-dependent energy deposition on the evolution of shells, which we discuss later.

The ambient ISM density $n_\circ$ can, in principal, be estimated from the amount of swept-up H I and therefore measured from the images (e.g. Ryder et al. 1995). However, lack of sensitivity to extended structure and the complexity of the small-scale structure in the images make meaningful estimates difficult for many shells in the SMC. Therefore, we only quote the ratio $L_s/n_\circ$ in Table 1.

The catalogued shells range in radius from 12 to 482 pc, in expansion velocity from 1.1 to 33.5 km s^{-1}, and in heliocentric velocity from 97 to 208 km s^{-1} (Table 1 and Fig. 7). As is the case with the LMC (Meaburn 1980), there is a clear separation between the six SMC supershells‡ with $r_s > 300$ pc (SMC HI-10, 20, 357, 454, 470 & 491) and the rest of the shells. These supershells exist in the outskirts and eastern Wing, well away from the stellar bar. The sharp drop in the number of shells with $r_s < 40$ pc (Fig. 7a) appears to be related to the limit of our spatial resolution (28 pc). The drop in the number of low-expansion-velocity shells ($v_s < 4$ km s^{-1}) (Fig. 7b) is probably not as affected by velocity resolution (1.5 km s^{-1}).

In age, the H I shells are remarkably tightly defined, with a total spread from 0.9 to 35.1 Myr only. Excluding the small number of shells with $T_s > 11$ Myr, the age distribution (Fig. 8a) has a mean $< T_s >= 5.4 \pm 0.1$ Myr and standard deviation 2.1 ± 0.1 Myr (distribution-independent standard errors are calculated following Kendall & Stuart 1963). The two oldest shells (SMC HI-16 & 52) reside in the south-west of the SMC, and there seems to be a tendency for shells in the southern part to be older on average by ~ 2.5 Myr. Only some of the age spread appears to result from observational errors. Taking into account the expected 21 per cent error in ages, the intrinsic dispersion in ages is 1.8 Myr.

The spread in wind luminosity $L_s(n_\circ/1 \text{ cm}^{-3})^{-1}$ (Fig. 8b) is $0.03L_\odot$ to $6\times10^5L_\odot$, over seven orders of magnitude. The least luminous shells have wind luminosities similar to those of single stars on the asymptotic giant branch (though the inferred ages and shell radii do not seem to be consistent with this origin). The highest luminosity shells, which require energy inputs $L_sT_s(n_\circ/1 \text{ cm}^{-3})^{-1} \approx 6 \times 10^{53}$ erg (Fig. 8c), can be powered only by winds and supernovae in OB associations originally containing $\sim 10^{2-3}$ O stars.

Unfortunately, we do not clearly identify any of the three supershells reported by Hindman (1967). The data for his largest shell look convincing, but its radius (54 arcmin) is too large for us to detect reliably. His second shell lies partly outside our images, and again its radius is large (45 arcmin). However, this shell is only 17 arcmin south of SMC-HI 10 in Table 1, so Hindman's shell is either associated with, or confused with SMC HI-10. SMC HI-10 has a heliocentric velocity of 139.1 km s^{-1} cf. 129 km s^{-1} for Hindman's shell; the expansion velocity is 28.3 km s^{-1} cf. 21 km s^{-1}; and the radius is 409 pc cf. 780 pc. The evidence for Hindman's third shell is less convincing. This shell is probably confused with SMC HI-491, though there are also other nearby massive shells in this region.

On the other hand, Meaburn's (1980) supershell SMC 1 is closely associated with SMC HI-498 at 173 km s^{-1}, al-

‡ There is good evidence for a continuous arc of H I joining the southern part of the bar to the eastern Wing. If interpreted as a seventh supershell, the radius would be ~ 1.2 kpc, and the centre would be at 01$^{\text{h}}$05$^{\text{m}}$, Dec $-73°50'$ (J2000) (this is not listed in Table 1). Against this interpretation is the fact that previous Parkes observations should have detected such an extended shell.

Table 1. List of positions, radii, expansion velocities, ages and required wind luminosity for the H I shells identified in the SMC.

SMC H I Shell	RA	DEC	Shell Radius		Heliocentric Velocity	Expansion Velocity	Age	Wind Luminosity
				r_s	V	v_s	T_s	$\log(L_s/n_o)$
	(J2000)		(′)	(pc)	(km s^{-1})		(10^6yr)	($L_\odot$ cm^3)
1	00:31:26	−72:52:24	2.7	47	121.4	5.9	4.7	1.52
2	00:32:07	−73:21:19	2.9	50	113.2	3.4	8.6	0.88
3	00:32:15	−72:49:46	1.3:	23	116.7:	2.5:	5.4	−0.19
4	00:33:07	−73:26:16	5.8	101	116.9	8.8	6.7	2.72
5	00:33:09	−73:23:17	2.4	43	121.8	8.8	2.8	1.97
6	00:33:19	−72:39:42	8.9	156	123.7	11.3	8.1	3.42
7	00:33:25	−72:56:19	4.9	86	123.9	8.4	6.1	2.51
8	00:34:10	−73:14:41	3.2	55	113.9	6.7	4.9	1.84
9	00:34:13	−72:58:10	11.3	197	144.0	25.8	4.5	4.69
10	00:34:33	−73:53:51	23.4	409	139.1	28.3	8.5	5.45
11	00:34:52	−72:31:19	6.1	106	138.9	14.4	4.3	3.40
12	00:34:57	−74:05:58	4.9	86	166.3	12.2	4.1	2.99
13	00:35:11	−73:19:36	7.5:	131	143.6	25.1	3.1	4.31
14	00:35:14	−73:06:06	1.9	34	119.5	10.2	1.9	1.95
15	00:35:18	−72:55:36	3.8:	66	110.3:	11.3:	3.4	2.67
16	00:35:34	−73:37:45	13.4	233	106.6	5.4	25.1	2.82
17	00:35:40	−71:23:34	6.8	118	155.9	16.1	4.3	3.64
18	00:36:19	−71:19:17	3.1	55	144.1	6.2	5.2	1.74
19	00:36:35	−74:21:30	6.2	108	162.5	5.6	11.2	2.19
20	00:37:08	−72:26:11	20.7	361	137.1	19.6	10.8	4.86
21	00:37:13	−70:59:55	11.6	202	137.3	26.0	4.6	4.73
22	00:37:17	−73:26:22	6.0	105	174.9	6.1	10.1	2.27
23	00:37:18	−72:57:51	2.5	43	129.1	8.0	3.2	1.85
24	00:37:58	−73:55:04	4.7	82	102.5	9.6	5.0	2.65
25	00:38:30	−71:41:21	6.8:	118	136.5:	14.4:	4.8	3.49
26	00:38:31	−74:47:28	14.0	244	146.6	13.5	10.6	4.04
27	00:38:41	−73:01:20	4.7	82	124.2	10.5	4.5	2.76
28	00:38:54	−74:13:17	6.2	108	158.9	4.5	14.0	1.90
29	00:39:12	−71:24:56	12.2	214	144.1	33.5	3.7	5.11
30	00:39:44	−73:46:38	4.5	78	125.7	16.3:	2.8	3.29
31	00:39:48	−73:19:41	3.3	58	115.5	5.0:	6.8	1.51
32	00:39:52	−74:13:34	2.5	43	123.0	3.8	6.7	0.86
33	00:39:56	−74:09:06	5.1	89	143.2	15.1	3.5	3.31
34	00:40:02	−74:59:47	2.8	49	135.0	2.9	9.8	0.65
35	00:40:09	−73:22:47	16.2	282	143.2	32.0	5.2	5.29
36	00:40:26	−71:13:13	5.8	101	139.7	17.6	3.4	3.62
37	00:40:26	−72:58:52	1.1	19	112.8	2.9	3.9	−0.15
38	00:40:28	−74:04:46	4.9	85	134.8	6.4	7.8	2.15
39	00:40:36	−73:43:53	6.9	121	111.5	6.7	10.5	2.51
40	00:40:40	−70:45:58	5.8	101	139.2	14.7	4.0	3.38
41	00:40:53	−73:34:59	2.2	39	109.0	2.9	7.8	0.45
42	00:41:04	−73:17:03	5.8	101	112.0	7.4	7.9	2.50
43	00:41:08	−73:51:30	2.0	35	113.0	8.4	2.4	1.73
44	00:41:20	−74:19:55	5.2	91	163.3	3.8	14.1	1.52
45	00:41:21	−73:26:07	5.0	87	169.9	7.6	6.7	2.40
46	00:41:23	−74:02:01	4.6	80	166.5	9.4	5.0	2.60
47	00:41:35	−73:27:41	2.5	43	108.6	5.4	4.6	1.34
48	00:41:36	−73:08:12	10.2	179	106.7	13.0	8.1	3.72
49	00:41:39	−73:00:43	3.3	58	117.3	6.5	5.2	1.84
50	00:41:40	−70:50:50	3.1	54	124.6	5.0	6.3	1.45
51	00:41:40	−71:07:32	1.3	23	115.8	1.7	8.1	−0.71
52	00:41:42	−74:45:20	12.9	225	134.0	3.8:	35.1	2.31
53	00:41:54	−72:45:45	5.8	102	143.1	8.5	7.0	2.68
54	00:41:57	−73:06:48	1.7	29	169.1	2.5	6.6	0.01
55	00:41:58	−73:20:17	2.9	51	173.3	2.9	10.1	0.68
56	00:42:07	−73:00:50	1.1	19	114.0	6.7	1.7	0.93
57	00:42:07	−73:33:48	3.8	66	114.7	10.1	3.9	2.52
58	00:42:22	−71:42:35	8.6:	150	141.8:	20.8:	4.2	4.18
59	00:42:25	−75:15:13	12.9	225	152.4	10.0	13.2	3.57
60	00:42:33	−74:03:48	2.0	35	113.2	5.9	3.5	1.27
61	00:42:39	−73:00:58	3.3	58	133.3	10.2	3.3	2.41
62	00:42:48	−73:29:29	1.8	31	100.6	5.4	3.4	1.07

Table 1 – *continued*

SMC H I Shell	RA	DEC	Shell Radius ($'$)	r_s (pc)	Heliocentric Velocity V (km s^{-1})	Expansion Velocity v_s (km s^{-1})	Age T_s (10^6yr)	Wind Luminosity $\log(L_s/n_o)$ ($L_\odot$ cm^3)
	(J2000)							
63	00:42:51	−73:48:56	2.6	45	115.2	4.5	5.9	1.15
64	00:42:54	−72:17:25	4.1	71	135.2	5.1	8.1	1.70
65	00:43:00	−73:13:03	5.5	96	130.7	10.7	5.3	2.92
66	00:43:03	−71:57:52	10.7	186	146.0	14.9	7.3	3.94
67	00:43:05	−73:44:30	6.7	117	100.6	11.3	6.0	3.17
68	00:43:13	−73:53:30	3.8	66	105.3:	8.8:	4.4	2.35
69	00:43:14	−71:26:10	3.4	59	158.1	8.1	4.3	2.14
70	00:43:24	−73:19:08	4.0	71	115.9	10.7	3.9	2.65
71	00:43:34	−72:41:40	1.0	17	150.1	1.8	5.4	−0.87
72	00:43:35	−74:05:32	7.7	134	144.4	20.8	3.8	4.08
73	00:43:36	−73:08:42	2.2	39	144.9	5.0	4.5	1.16
74	00:43:37	−74:26:24	4.9	85	130.3	6.0	8.3	2.07
75	00:43:40	−71:33:50	1.7	30	168.2	3.0	5.8	0.23
76	00:43:46	−72:32:41	1.6	27	160.6	2.9	5.4	0.15
77	00:43:59	−74:33:55	5.2	91	138.3	5.3	10.1	1.96
78	00:44:00	−72:28:14	3.5	61	143.3	18.1	2.0	3.21
79	00:44:00	−73:04:17	9.6	168	133.0	16.0	6.2	3.93
80	00:44:03	−73:13:17	4.5:	79	129.6	22.8	2.0	3.74
81	00:44:10	−73:56:41	2.3	40	142.9	24.9	0.9	3.26
82	00:44:12	−73:52:13	2.2	39	121.4:	3.4:	6.8	0.63
83	00:44:14	−72:34:18	2.7	47	152.8	11.4	2.4	2.39
84	00:44:23	−71:29:29	1.9	34	131.9	4.8	4.2	0.96
85	00:44:27	−71:40:05	1.8	31	129.1	2.9	6.2	0.25
86	00:44:30	−73:11:53	3.1	54	120.5	7.5	4.2	1.98
87	00:44:36	−72:44:54	7.3	127	140.1	10.0	7.5	3.08
88	00:44:37	−72:38:54	5.1	89	151.7	10.3	5.1	2.81
89	00:44:46	−74:17:42	3.9	68	132.6	4.5	8.8	1.51
90	00:44:47	−73:49:21	2.7	47	97.0	2.9	9.3	0.61
91	00:44:52	−73:32:55	5.0	87	117.1	7.2	7.1	2.33
92	00:44:55	−73:17:58	3.8	66	98.8	7.1	5.4	2.07
93	00:44:56	−73:08:59	2.2	39	108.8	4.6	4.9	1.04
94	00:44:58	−74:25:11	2.2	39	134.3	2.1	10.9	0.01
95	00:45:16	−72:28:30	4.5	78	122.9	8.9	5.2	2.50
96	00:45:21	−73:30:01	5.6	97	142.1	13.4	4.2	3.23
97	00:45:24	−74:07:22	2.0	34	166.6	2.3	8.8	0.00
98	00:45:25	−72:54:04	2.9	51	161.3	4.1	7.4	1.11
99	00:45:36	−71:29:45	15.2	266	161.1	13.9	11.2	4.15
100	00:45:44	−73:24:06	4.9	86	167.7	9.5	5.3	2.67
101	00:45:44	−73:37:34	8.2	144	115.9	9.6	8.7	3.14
102	00:45:45	−72:21:04	8.5:	148	123.8:	12.2:	7.1	3.47
103	00:45:53	−73:09:09	2.4	43	125.8	6.3	4.0	1.53
104	00:45:57	−73:45:05	2.7	47	127.5	14.7	1.9	2.71
105	00:45:58	−72:39:09	2.0	35	125.2	8.8:	2.3	1.79
106	00:46:09	−73:01:43	4.7	82	99.4	9.2	5.2	2.59
107	00:46:10	−73:12:12	3.3	58	126.2:	30.1:	1.1	3.83
108	00:46:13	−73:27:11	5.6	97	112.6	18.4	3.1	3.64
109	00:46:15	−72:13:38	4.5	79	141.9	16.4	2.8	3.31
110	00:46:33	−73:06:17	4.0	71	154.2	12.7	3.3	2.88
111	00:46:36	−73:18:16	6.5	113	118.7	12.2	5.4	3.23
112	00:46:36	−74:43:18	4.5	78	135.9	7.6	6.0	2.30
113	00:46:40	−72:57:18	2.2	39	113.9	6.7	3.4	1.53
114	00:46:44	−72:40:48	2.4	42	161.5	4.8	5.2	1.17
115	00:46:46	−73:04:49	2.5	43	116.1	5.9	4.3	1.44
116	00:46:47	−72:57:19	4.1	72	168.9	4.7	8.9	1.61
117	00:46:57	−71:48:08	3.3	58	132.9	14.6	2.3	2.88
118	00:46:57	−72:51:21	4.4	76	147.4	10.0	4.5	2.63
119	00:47:01	−74:34:27	5.6	97	96.6	11.2	5.1	3.00
120	00:47:17	−72:46:54	3.9	68	133.9	8.1	4.9	2.27
121	00:47:17	−72:55:54	3.2	55	111.4	5.5	5.9	1.59
122	00:47:24	−73:58:45	5.2	91	168.3	6.4	8.3	2.21
123	00:47:29	−73:24:24	3.1	54	172.8	10.1	3.2	2.35
124	00:47:40	−73:31:54	4.2	74	147.9	5.0	8.6	1.71

Table 1 – *continued*

SMC H I Shell	RA	DEC	Shell Radius		Heliocentric Velocity	Expansion Velocity	Age	Wind Luminosity
				r_s	V	v_s	T_s	$\log(L_s/n_0)$
	(J2000)		(′)	(pc)	(km s^{-1})		(10^6yr)	($L_\odot$ cm^3)
125	00:47:42	−72:28:56	3.7	65	148.5	4.8	8.0	1.54
126	00:47:42	−73:10:57	9.0	157	143.5	15.1	6.1	3.80
127	00:47:55	−72:30:28	2.9	51	133.2	5.5	5.4	1.52
128	00:47:56	−73:01:59	2.7	47	114.6:	13.4:	2.0	2.59
129	00:47:58	−72:24:27	10.7:	187	154.3:	11.8:	9.3	3.63
130	00:48:04	−72:03:23	1.7	29	134.9	6.6	2.6	1.25
131	00:48:07	−73:17:00	2.6	45	166.4	5.2	5.1	1.34
132	00:48:10	−73:55:52	2.6	45	169.3	3.8	7.1	0.92
133	00:48:15	−73:31:59	5.8	101	130.1	9.6	6.1	2.83
134	00:48:24	−73:18:32	7.2	126	147.7	12.6	5.8	3.38
135	00:48:27	−72:12:29	5.2	91	149.3	11.9	4.5	3.01
136	00:48:42	−73:02:06	7.4	129	151.8	11.2	6.7	3.25
137	00:48:45	−72:41:06	2.2	38	137.5	8.9	2.5	1.88
138	00:48:45	−72:54:36	2.2	38	149.5	7.7	2.9	1.70
139	00:49:00	−73:05:08	4.9	86	179.7	6.5	7.7	2.19
140	00:49:05	−71:30:20	1.2:	21	153.6:	2.2:	5.6	−0.45
141	00:49:08	−72:59:09	4.1	72	166.0	6.9	6.1	2.10
142	00:49:11	−72:51:39	3.4	59	109.9	5.5	6.3	1.65
143	00:49:12	−73:29:06	7.3	128	174.4	11.3	6.6	3.25
144	00:49:15	−72:27:38	9.2:	161	103.5:	25.8:	3.6	4.52
145	00:49:15	−72:33:39	3.6	62	114.5	16.3	2.2	3.10
146	00:49:21	−71:40:56	3.3	58	154.8	8.4	4.0	2.16
147	00:49:26	−72:50:11	6.8	119	130.0	14.4	4.8	3.50
148	00:49:33	−72:26:10	2.5	43	150.0	5.9	4.3	1.46
149	00:49:43	−73:41:07	9.6	167	163.2	12.6	7.8	3.62
150	00:49:48	−73:18:42	5.3	93	180.3	8.0	6.9	2.52
151	00:49:49	−73:17:12	3.2	55	152.8	11.5	2.8	2.55
152	00:49:56	−72:32:13	1.7	30	138.1	12.2	1.4	2.07
153	00:50:01	−72:23:12	7.0	122	121.1	10.0	7.2	3.04
154	00:50:13	−72:53:16	2.7	47	117.9	4.4	6.2	1.15
155	00:50:15	−71:19:53	2.0	35	161.6	4.6	4.4	0.95
156	00:50:25	−72:51:47	3.7	64	170.2	3.7	10.1	1.18
157	00:50:27	−73:32:13	6.0	105	156.1	11.4	5.4	3.09
158	00:50:28	−72:48:47	2.9	51	115.9	3.3	9.0	0.85
159	00:50:32	−72:56:18	5.8	102	136.5	10.3	5.8	2.93
160	00:50:36	−71:33:31	3.6	63	147.6	9.2	4.0	2.36
161	00:50:41	−73:09:48	8.6	150	160.8	16.0	5.5	3.83
162	00:50:46	−73:18:47	9.1	159	128.1	17.6	5.3	4.01
163	00:50:55	−72:35:19	5.8	102	162.0	10.7	5.6	2.98
164	00:51:08	−72:42:51	7.3	127	162.3	12.2	6.1	3.34
165	00:51:10	−72:45:51	5.8	102	105.4	12.9	4.6	3.22
166	00:51:15	−71:23:00	2.9	51	160.0	6.2	4.8	1.67
167	00:51:16	−73:44:14	4.9	86	116.8	19.7	2.5	3.62
168	00:51:17	−73:26:18	2.4	43	175.7	8.4:	3.0	1.90
169	00:51:20	−72:48:52	2.9	51	131.0	11.1	2.7	2.42
170	00:51:23	−72:06:46	3.8	67	162.3	11.7	3.3	2.72
171	00:51:25	−72:27:51	3.2:	56	140.6:	25.8:	1.3	3.61
172	00:51:32	−73:00:52	4.4	77	174.9	5.8	7.7	1.93
173	00:51:33	−71:53:13	2.8	49	167.6	6.6	4.4	1.70
174	00:51:33	−72:57:53	2.9	51	145.1	10.5	2.8	2.34
175	00:51:34	−71:15:27	3.1	55	157.0	5.9	5.5	1.66
176	00:51:46	−73:06:53	6.3	110	176.2	8.7	7.4	2.78
177	00:51:53	−74:11:07	10.7	187	156.1	22.2	4.9	4.46
178	00:52:01	−72:21:52	7.0	122	145.2	21.0	3.4	4.01
179	00:52:02	−73:33:50	7.6	132	134.2	13.4	5.8	3.50
180	00:52:10	−72:57:55	6.0	106	113.6	6.2	10.0	2.29
181	00:52:17	−73:18:53	3.3	58	177.8	3.8	9.1	1.13
182	00:52:26	−71:10:58	2.4	42	151.0	2.9	8.4	0.53
183	00:52:38	−72:23:24	3.5	61	173.0	6.6	5.4	1.91
184	00:52:38	−73:00:56	4.1	72	159.3	9.1	4.6	2.46
185	00:52:43	−73:00:56	7.3	128	132.5	13.0	5.8	3.43
186	00:52:55	−73:23:24	2.5	43	144.8	5.9	4.3	1.44

Table 1 – *continued*

SMC H I Shell	RA	DEC	Shell Radius		Heliocentric Velocity	Expansion Velocity	Age	Wind Luminosity
				r_s	V	v_s	T_s	$\log(L_s/n_0)$
	(J2000)		(′)	(pc)	(km s^{-1})		(10^6yr)	($L_\odot$ cm^3)
187	00:52:55	−73:26:24	2.9	51	146.6	5.4	5.4	1.49
188	00:53:06	−72:47:28	5.8	102	137.8	14.4	4.2	3.36
189	00:53:11	−73:39:51	2.9	51	133.1	3.4	8.8	0.88
190	00:53:12	−73:29:24	5.3	93	139.5	9.9	5.5	2.80
191	00:53:13	−71:50:18	2.8	49	164.2	5.8	4.9	1.54
192	00:53:14	−73:53:18	12.2:	214	173.8:	10.5:	12.0	3.59
193	00:53:19	−72:35:28	3.4	59	150.2	10.7	3.3	2.51
194	00:53:31	−72:48:59	5.1:	89	174.2:	8.8:	6.0	2.61
195	00:53:35	−72:36:58	8.5	149	119.3	19.2	4.5	4.07
196	00:53:39	−71:45:47	9.9	173	156.0	15.7	6.5	3.93
197	00:53:43	−73:14:27	3.1:	54	163.0:	5.0:	6.3	1.45
198	00:53:51	−73:02:29	3.3	58	162.1	6.9	4.9	1.91
199	00:54:00	−72:18:57	7.9	137	127.4	12.0	6.7	3.39
200	00:54:01	−72:54:59	2.4	42	128.9	4.1	6.1	0.95
201	00:54:04	−73:29:25	8.7	151	163.5	14.5	6.1	3.71
202	00:54:07	−72:06:54	2.1	37	169.9	4.0	5.5	0.83
203	00:54:07	−72:44:29	5.1	89	108.1	14.7	3.5	3.28
204	00:54:13	−71:51:50	1.8	31	170.9	5.1	3.6	0.98
205	00:54:17	−72:29:28	3.7	65	134.1	7.4	5.2	2.11
206	00:54:19	−71:30:42	7.5	131	159.1	10.6	7.2	3.19
207	00:54:21	−73:00:59	4.7	82	175.2	7.6	6.3	2.34
208	00:54:25	−72:27:58	1.7	30	173.5	5.9	3.0	1.15
209	00:54:27	−72:21:58	1.7	30	154.0	5.5	3.2	1.07
210	00:54:46	−72:12:56	7.4	129	149.9	14.6	5.2	3.58
211	00:54:48	−71:12:33	6.3	110	151.9	8.8	7.3	2.79
212	00:54:52	−72:24:58	3.7	65	161.3	5.5	6.9	1.73
213	00:55:02	−72:46:00	2.9	51	181.9	5.4	5.4	1.49
214	00:55:03	−71:06:30	1.9	34	159.0	2.9	6.7	0.33
215	00:55:06	−73:14:28	3.6	62	185.1	6.9	5.3	1.98
216	00:55:12	−71:53:21	3.8	66	165.4	12.0	3.2	2.76
217	00:55:16	−73:20:27	4.2	74	179.4	8.8	4.9	2.44
218	00:55:48	−72:32:29	5.1	89	170.0	6.6	7.9	2.24
219	00:55:55	−71:44:17	5.6	97	164.5	7.7	7.5	2.50
220	00:56:00	−72:42:59	4.1	72	162.9	10.3	4.1	2.63
221	00:56:01	−72:11:25	1.2	21	160.4	2.2	5.6	−0.47
222	00:56:19	−72:18:56	2.4	43	130.6	9.6:	2.6	2.09
223	00:56:19	−72:21:57	2.2	39	131.5	4.1	5.6	0.88
224	00:56:19	−72:56:29	8.5	149	161.7	24.3	3.6	4.38
225	00:56:24	−70:48:17	0.7	13	117.7	1.5	5.1	−1.42
226	00:56:35	−72:23:26	4.0	70	146.2	15.5	2.6	3.13
227	00:56:39	−73:08:27	10.2	177	163.3	29.4	3.5	4.78
228	00:56:45	−72:00:51	4.1	71	160.5	6.6	6.3	2.02
229	00:56:47	−71:39:44	1.0	18	156.8	1.5	7.1	−1.14
230	00:56:53	−72:50:28	6.3	110	150.3	15.1	4.3	3.50
231	00:57:00	−72:53:27	7.5	132	110.2	19.2	4.0	3.96
232	00:57:02	−71:11:00	1.7	30	151.2	3.3	5.2	0.37
233	00:57:03	−72:33:57	3.2	55	130.8	4.8	6.8	1.40
234	00:57:04	−71:35:12	2.7	46	156.1	3.7	7.3	0.91
235	00:57:08	−72:57:57	5.2	91	182.0	11.2	4.7	2.94
236	00:57:11	−72:42:57	5.8	102	184.6	10.0	6.0	2.88
237	00:57:13	−72:17:24	2.0	35	125.1	4.6	4.4	0.95
238	00:57:18	−72:50:27	2.4	42	165.0	5.2	4.8	1.27
239	00:57:20	−73:24:53	2.6	45	169.1	12.9	2.1	2.52
240	00:57:21	−72:06:51	1.9	33	168.0	3.3	5.9	0.47
241	00:57:26	−72:24:54	2.2	39	122.2	10.1:	2.3	2.06
242	00:57:30	−71:29:08	4.4	76	141.8	8.8	5.1	2.47
243	00:57:39	−72:08:21	3.1	54	133.0	16.4	1.9	2.98
244	00:57:42	−72:11:21	5.7	100	165.3	15.7	3.7	3.46
245	00:57:53	−71:48:44	4.7	82	153.9	9.6	5.0	2.65
246	00:57:54	−72:12:51	1.8	31	183.5	2.5	7.2	0.06
247	00:57:55	−71:10:57	2.2	39	151.4	2.1	10.9	0.01
248	00:57:56	−71:12:28	6.3	110	160.9	9.2	7.0	2.84

Table 1 – *continued*

SMC H I Shell	RA	DEC	Shell Radius	r_s	Heliocentric Velocity V	Expansion Velocity v_s	Age T_s	Wind Luminosity $\log(L_s/n_o)$
	(J2000)		(′)	(pc)	(km s^{-1})		(10^6yr)	($L_\odot$ cm^3)
249	00:58:08	−72:44:24	4.6	81	169.4	7.0	6.7	2.22
250	00:58:09	−71:20:01	4.2	74	135.9	11.3:	3.8	2.77
251	00:58:11	−73:03:53	2.2	38	185.3	6.5	3.4	1.48
252	00:58:18	−71:53:14	4.3	75	173.8	12.4	3.6	2.91
253	00:58:24	−72:48:53	2.7	47	179.5	6.3	4.3	1.61
254	00:58:29	−72:24:51	4.0	70	154.0	21.0	1.9	3.53
255	00:58:33	−72:30:51	6.8	119	161.8	10.7	6.5	3.11
256	00:58:40	−71:57:44	3.5	62	166.8	5.5	6.5	1.69
257	00:58:45	−72:21:49	3.5	61	130.8	5.9	6.0	1.75
258	00:58:49	−71:53:12	1.3	22	156.8	8.4	1.6	1.33
259	00:58:49	−72:57:51	2.5	43	190.2	4.0	6.3	0.95
260	00:58:52	−72:59:21	9.3	163	129.5	14.9	6.4	3.81
261	00:58:52	−73:54:40	4.2	74	165.9	7.5	5.7	2.24
262	00:58:54	−72:44:21	2.9	51	138.0	5.2	5.8	1.43
263	00:58:55	−72:06:45	1.1	19	171.3	2.9	3.9	−0.15
264	00:59:00	−72:27:49	3.0	52	153.3	17.7	1.7	3.05
265	00:59:06	−73:14:18	2.7	48	160.1	16.3	1.7	2.87
266	00:59:08	−71:45:37	2.3	40	171.5	13.1	1.8	2.43
267	00:59:11	−72:50:19	3.6	62	150.3	8.8	4.1	2.29
268	00:59:11	−73:00:49	2.2	38	189.0	4.7	4.8	1.06
269	00:59:23	−73:15:47	3.2	55	180.8	6.0	5.5	1.68
270	00:59:39	−72:27:45	2.7	48	182.3	6.3	4.5	1.62
271	00:59:56	−72:38:15	5.4	93	182.2	10.0	5.5	2.81
272	00:59:58	−71:41:01	2.9	51	160.8	4.6	6.4	1.27
273	01:00:05	−72:39:44	2.4	42	147.1	7.0	3.6	1.67
274	01:00:09	−71:25:53	3.9	68	151.8	5.5:	7.2	1.75
275	01:00:20	−71:15:16	3.3	58	151.1	8.8	3.9	2.24
276	01:00:25	−71:22:50	4.1	72	170.5	8.1	5.2	2.30
277	01:00:26	−71:06:10	1.4	25	162.6	4.0	3.7	0.50
278	01:00:26	−71:56:03	8.4	146	182.0	14.9	5.7	3.73
279	01:00:26	−72:05:06	5.0	87	168.5	8.7	5.9	2.58
280	01:00:28	−72:50:12	6.5	113	194.3	9.2	7.2	2.87
281	01:00:35	−73:38:06	4.7	82	177.1	10.5	4.6	2.76
282	01:00:37	−73:32:07	4.0	70	149.4	6.1	6.7	1.92
283	01:00:38	−72:57:41	3.0	53	191.1	4.0	7.7	1.12
284	01:00:39	−73:29:07	12.3	215	165.4	20.2	6.3	4.45
285	01:00:46	−72:09:34	11.1	194	129.5	17.2	6.6	4.15
286	01:00:49	−71:13:42	1.9	34	156.4	4.0	4.9	0.75
287	01:01:05	−71:39:22	3.1	54	150.9	7.1	4.5	1.90
288	01:01:09	−72:24:35	3.8	67	175.8	9.3	4.2	2.43
289	01:01:12	−71:10:37	4.4	76	173.4	11.4	3.9	2.80
290	01:01:12	−71:52:56	2.3	40	167.6	4.4	5.3	1.00
291	01:01:16	−72:57:36	2.7	48	139.2	10.5	2.7	2.30
292	01:01:27	−73:54:25	5.2	91	169.7	8.7	6.1	2.60
293	01:01:29	−71:57:26	11.9	208	148.7	21.1	5.8	4.48
294	01:01:30	−73:24:32	3.3	58	139.7	8.4	4.1	2.17
295	01:01:32	−73:02:04	0.7:	12	202.9:	1.7:	4.1	−1.32
296	01:01:46	−72:35:01	4.4	76	198.9	6.6	6.7	2.10
297	01:01:53	−73:00:31	3.3	58	190.1	10.2	3.3	2.41
298	01:01:56	−70:55:21	4.8	84	161.9	7.0	7.1	2.26
299	01:02:02	−72:40:59	16.5:	288	104.0:	15.5:	10.9	4.36
300	01:02:05	−72:24:27	15.7	274	156.7	27.7	5.8	5.07
301	01:02:07	−71:40:44	5.1	89	167.1	6.6	7.9	2.22
302	01:02:11	−71:07:26	3.1	55	165.1	5.5	5.8	1.57
303	01:02:11	−71:27:07	5.1	89	166.2	9.5	5.4	2.71
304	01:02:15	−72:18:24	8.5	148	174.3	12.2	7.1	3.47
305	01:02:23	−71:45:13	3.3	58	167.1	8.0	4.2	2.11
306	01:02:40	−72:57:24	4.9	86	192.5	8.4	6.1	2.51
307	01:02:44	−73:19:52	3.2	55	153.0	9.5	3.4	2.30
308	01:02:51	−72:37:52	3.7	64	184.4	4.8	7.8	1.52
309	01:03:03	−72:03:13	3.6	62	181.0	6.9	5.3	1.98
310	01:03:04	−72:12:15	9.5	166	155.1	17.5	5.6	4.04

Table 1 – *continued*

SMC H I Shell	RA	DEC	Shell Radius		Heliocentric Velocity	Expansion Velocity	Age	Wind Luminosity
				r_s	V	v_s	T_s	$\log(L_s/n_o)$
	(J2000)		(′)	(pc)	(km s^{-1})		(10^6yr)	($L_\odot$ cm^3)
311	01:03:10	−71:58:40	3.3	58	182.0	4.7	7.2	1.43
312	01:03:15	−72:45:18	2.4:	42	146.9	23.6	1.1	3.25
313	01:03:30	−72:40:45	4.0	70	124.6	4.6	8.9	1.55
314	01:03:50	−74:41:45	1.3	23	152.9	2.3	5.9	−0.35
315	01:04:02	−73:00:11	4.1	72	161.1	8.7	4.8	2.41
316	01:04:04	−71:38:53	8.1	142	184.5	16.8	5.0	3.85
317	01:04:06	−72:15:05	2.1	37	181.4	4.4	5.0	0.94
318	01:04:20	−72:55:37	2.7	47	194.6	5.9	4.6	1.52
319	01:04:40	−71:53:51	2.5	44	175.3	7.3	3.6	1.75
320	01:04:40	−71:59:54	6.2	108	171.1	10.9	5.8	3.06
321	01:04:42	−72:37:32	2.4	43	121.9	8.0	3.1	1.84
322	01:04:45	−72:08:55	2.1	37	148.3	18.2	1.2	2.80
323	01:04:52	−73:12:01	3.0	53	156.1	4.7	6.6	1.34
324	01:04:59	−72:05:52	6.4	112	181.4	14.9	4.4	3.50
325	01:05:03	−71:47:44	2.8	49	181.4	5.1	5.6	1.37
326	01:05:05	−72:44:58	3.9:	68	149.3	25.8	1.5	3.77
327	01:05:08	−73:05:58	3.3	58	170.0	13.4	2.5	2.78
328	01:05:15	−73:23:55	4.6	81	175.0	11.8	4.0	2.90
329	01:05:18	−72:34:24	2.9	51	139.4	12.6	2.4	2.58
330	01:05:23	−72:38:53	4.2	74	146.6	18.9	2.3	3.44
331	01:05:29	−71:24:58	6.0	105	174.3	8.0	7.7	2.62
332	01:05:30	−72:41:52	6.3	110	181.9	10.3	6.3	3.00
333	01:05:30	−73:23:52	9.1	159	151.0	13.8	6.8	3.70
334	01:05:38	−71:56:40	2.5	43	188.6	15.5	1.6	2.71
335	01:05:50	−71:56:37	4.0	70	163.5	8.8	4.7	2.40
336	01:05:50	−72:29:46	2.9	51	175.5	5.2	5.8	1.43
337	01:05:58	−71:44:31	2.5	44	199.6	14.6	1.8	2.66
338	01:05:58	−72:44:47	2.9	51	153.0	14.0	2.1	2.73
339	01:06:03	−71:30:53	2.9	51	175.3	5.5	5.4	1.50
340	01:06:06	−72:59:46	4.2	74	157.8	7.5	5.7	2.24
341	01:06:10	−72:32:42	2.4	42	135.6	5.5	4.5	1.36
342	01:06:31	−71:06:32	7.0	122	173.1	12.1	5.9	3.30
343	01:06:32	−72:55:09	5.4	93	185.9	7.0	7.8	2.35
344	01:06:46	−72:25:02	5.7	100	182.2	11.8	5.0	3.09
345	01:06:59	−71:56:21	2.4	43	194.5	6.3	4.0	1.53
346	01:06:59	−73:08:33	2.0	35	186.8	5.0	4.1	1.06
347	01:07:04	−71:33:39	6.0	106	168.0	10.0	6.2	2.92
348	01:07:07	−72:03:51	4.0	70	167.9	5.4	7.5	1.77
349	01:07:09	−73:08:31	2.8	49	170.2	6.5	4.4	1.69
350	01:07:11	−72:00:49	6.4	112	186.8	12.8	5.2	3.29
351	01:07:18	−72:47:28	2.4	42	141.9	12.5	2.0	2.42
352	01:07:19	−73:00:59	2.2	39	184.2	3.8	6.0	0.78
353	01:07:22	−71:51:43	3.8	66	185.8	8.4	4.6	2.28
354	01:07:25	−72:54:57	1.6	27	191.1	4.2	3.8	0.61
355	01:07:30	−72:21:50	10.2	179	135.9	13.0	8.1	3.72
356	01:07:32	−73:15:55	4.0	70	171.5	10.9	3.8	2.67
357	01:07:33	−72:08:16	21.9	383	107.5	26.6:	8.4	5.31
358	01:07:33	−72:39:53	4.4	76	156.5	19.9	2.2	3.54
359	01:07:39	−71:16:50	4.1	72	180.7	11.0	3.8	2.71
360	01:07:42	−72:41:21	5.1	89	188.7	10.7	4.9	2.86
361	01:08:02	−71:37:55	1.3:	23	195.6:	2.5:	5.4	−0.19
362	01:08:07	−72:08:07	2.6	46	133.4	3.6	7.4	0.88
363	01:08:08	−72:20:10	2.7	48	179.3	4.1	6.9	1.06
364	01:08:12	−71:48:28	5.1	89	190.5	8.8	5.9	2.59
365	01:08:20	−71:46:55	3.6	62	205.1	7.3	5.0	2.05
366	01:08:36	−72:04:58	3.1	54	186.2	6.2	5.1	1.71
367	01:08:43	−72:38:04	4.0	70	125.4	11.3	3.6	2.72
368	01:08:48	−73:08:05	5.3	93	181.9	8.8	6.2	2.65
369	01:08:53	−71:24:03	2.2	38	117.7	2.6:	8.7	0.26
370	01:09:15	−72:52:57	3.4	59	161.1	12.9	2.7	2.75
371	01:09:16	−72:07:47	8.9	156	200.3	10.5:	8.7	3.32
372	01:09:19	−71:37:33	6.3	111	184.0	17.1	3.8	3.66

Table 1 – *continued*

SMC H I Shell	RA	DEC	Shell Radius		Heliocentric Velocity	Expansion Velocity	Age	Wind Luminosity
				r_s	V	v_s	T_s	$\log(L_s/n_0)$
	(J2000)		(′)	(pc)	(km s^{-1})		(10^6yr)	($L_\odot$ cm^3)
373	01:09:20	−73:01:56	5.1	89	123.6	13.4:	3.9	3.16
374	01:09:21	−72:48:25	1.7	30	186.8	4.1	4.3	0.64
375	01:09:27	−73:15:24	8.4	146	160.4	13.4	6.4	3.58
376	01:09:29	−72:57:23	8.2	144	192.1	12.7	6.6	3.50
377	01:09:37	−71:54:05	3.1	54	188.3	8.0	4.0	2.05
378	01:09:38	−71:55:35	13.7	238	152.9	22.9	6.1	4.71
379	01:09:53	−72:31:42	16.5	289	156.2	23.6	7.2	4.91
380	01:10:01	−71:47:55	10.9	191	174.2	10.1	11.1	3.44
381	01:10:07	−72:40:40	5.1	89	161.0	25.8:	2.0	4.01
382	01:10:14	−72:48:09	3.3	58	198.7	5.4	6.3	1.61
383	01:10:17	−72:46:38	5.8	102	178.8	12.2	4.9	3.14
384	01:10:22	−72:19:30	4.0	70	175.8	6.6	6.1	2.02
385	01:10:26	−71:12:56	1.3	23	145.2	4.2	3.3	0.48
386	01:10:31	−73:03:05	3.8	67	175.7	6.5	6.0	1.97
387	01:10:33	−73:01:34	4.9	86	145.0	17.0	3.0	3.44
388	01:10:38	−71:44:41	1.3:	23	199.8:	2.1:	6.5	−0.43
389	01:10:46	−71:52:12	1.8	31	200.6	4.2	4.4	0.72
390	01:11:00	−72:10:14	14.5	254	156.4	22.6	6.6	4.74
391	01:11:19	−73:10:20	6.0	105	175.7	8.1	7.6	2.64
392	01:11:26	−71:04:59	16.7	291	176.6	20.2	8.5	4.72
393	01:11:44	−72:55:11	1.9	34	139.5	5.8	3.4	1.22
394	01:11:53	−72:43:06	6.8	119	148.6	14.0	5.0	3.46
395	01:11:59	−72:31:01	1.9	34	178.7	2.6	7.7	0.17
396	01:11:59	−73:07:07	4.8	84	165.6	6.9	7.1	2.23
397	01:12:10	−72:36:59	11.9	208	191.5	17.7	6.9	4.25
398	01:12:23	−73:28:00	9.7	169	174.6	14.5	6.8	3.81
399	01:12:24	−72:20:19	3.7	65	132.8	6.3	6.1	1.89
400	01:12:29	−72:06:42	5.7	100	177.7	6.2	9.5	2.25
401	01:12:39	−72:21:44	7.2	126	156.2	17.3	4.3	3.79
402	01:12:47	−72:26:12	6.5	113	171.0	8.8	7.5	2.81
403	01:12:49	−73:23:21	8.4	146	144.0	21.3	4.0	4.19
404	01:12:57	−72:23:08	12.9	226	191.4	17.3	7.6	4.30
405	01:13:01	−72:17:04	2.6	46	175.9	3.3	8.2	0.74
406	01:13:26	−72:10:52	4.1	71	194.2	11.7	3.6	2.77
407	01:13:29	−73:03:35	8.8	153	180.4	7.3	12.4	2.83
408	01:13:30	−73:03:35	12.9:	225	119.3:	13.4:	9.9	3.96
409	01:13:39	−73:15:32	2.3	40	168.3	3.7	6.4	0.79
410	01:14:25	−71:53:51	8.6	151	159.6	19.3	4.6	4.09
411	01:14:25	−72:54:12	3.8	67	148.4	9.4	4.2	2.45
412	01:14:47	−73:42:07	1.3	23	195.6	3.4	4.1	0.19
413	01:14:53	−71:14:13	4.4	76	164.9	25.7:	1.7	3.86
414	01:14:53	−73:15:04	3.8	66	176.9	5.6	6.9	1.75
415	01:14:54	−72:46:29	13.1	229	116.1	27.3:	4.9	4.90
416	01:14:56	−71:09:39	4.1	72	154.4	18.3	2.3	3.37
417	01:15:00	−72:17:47	6.0	104	199.1	9.2	6.6	2.80
418	01:15:00	−72:29:52	1.5	25	174.3	3.0	5.1	0.10
419	01:15:02	−72:59:59	8.2	144	123.2:	16.3:	5.2	3.83
420	01:15:04	−72:38:53	8.0	140	135.0	13.0	6.3	3.51
421	01:15:05	−71:35:23	14.3	249	204.4	13.0:	11.2	4.01
422	01:15:11	−71:06:29	0.9:	16	175.5:	1.7:	5.5	−1.07
423	01:15:29	−73:23:51	3.1	54	177.3	6.3	5.1	1.74
424	01:15:34	−73:31:19	3.9	68	179.5	6.8	5.9	2.03
425	01:15:40	−71:53:19	9.4	164	194.7	14.9	6.4	3.82
426	01:15:49	−71:45:40	2.2	39	192.0	4.2	5.4	0.92
427	01:15:53	−72:02:18	9.8	171	180.7	21.1	4.7	4.31
428	01:16:00	−71:47:06	4.9	86	206.8	9.6:	5.2	2.69
429	01:16:02	−72:23:23	4.7	83	164.0	18.8	2.6	3.53
430	01:16:05	−73:50:36	9.1	159	170.4	31.6	2.9	4.78
431	01:16:11	−72:48:57	2.4	42	145.2	3.7	6.7	0.83
432	01:16:21	−73:28:00	3.3	58	143.3	8.8	3.9	2.24
433	01:16:26	−72:53:22	5.5	96	155.7	12.3	4.6	3.11
434	01:16:45	−72:51:44	6.3	110	176.9	7.0	9.2	2.50

Table 1 – *continued*

SMC H I Shell	RA	DEC	Shell Radius		Heliocentric Velocity	Expansion Velocity	Age	Wind Luminosity
				r_s	V	v_s	T_s	$\log(L_s/n_\circ)$
	(J2000)		(′)	(pc)	(km s^{-1})		(10^6yr)	($L_\odot$ cm^3)
435	01:17:15	−71:48:02	7.1	124	191.6	13.1	5.5	3.41
436	01:17:18	−72:57:31	1.9	34	140.7	3.6	5.4	0.60
437	01:17:20	−73:45:35	9.4	165	183.5	12.1	8.0	3.55
438	01:17:21	−72:24:18	4.7	83	189.7	10.7	4.5	2.79
439	01:17:27	−71:38:50	4.8	84	193.1	10.6	4.7	2.79
440	01:17:27	−73:12:30	5.8	101	142.2	7.1	8.4	2.43
441	01:17:32	−71:08:24	6.8	118	191.2	13.6	5.1	3.42
442	01:17:40	−73:22:55	5.8	101	182.5	17.9	3.3	3.64
443	01:17:47	−72:02:55	3.3	58	186.1	8.4	4.1	2.17
444	01:17:56	−73:21:18	14.7	257	164.0	24.7	6.1	4.87
445	01:18:01	−72:33:03	5.6	98	159.3	21.8	2.6	3.87
446	01:18:07	−74:13:43	6.0	105	166.3	22.2	2.8	3.95
447	01:18:13	−71:24:47	5.3	93	208.1	8.1	6.7	2.53
448	01:18:15	−73:27:10	4.2	74	145.2	9.6	4.5	2.56
449	01:18:28	−72:52:27	2.2	38	154.2	10.9	2.1	2.15
450	01:18:39	−72:47:50	3.6	64	176.0	5.5	6.7	1.71
451	01:18:45	−71:42:44	3.8	66	202.9	6.6	5.9	1.97
452	01:19:04	−72:05:19	2.7	47	186.0	10.9	2.5	2.32
453	01:19:07	−72:23:27	5.7	100	178.2	10.0	5.9	2.87
454	01:19:11	−73:11:41	20.3	354	164.8	24.7	8.4	5.15
455	01:19:17	−73:07:07	10.5	183	176.9	21.0	5.1	4.36
456	01:19:31	−73:05:30	4.5	79	147.0	7.0	6.6	2.20
457	01:19:40	−72:33:45	6.3	110	193.0	15.5	4.2	3.53
458	01:19:54	−73:23:23	2.0	35	140.6	3.8	5.4	0.69
459	01:20:05	−74:35:18	2.5	43	185.3:	5.4:	4.6	1.34
460	01:20:07	−72:54:39	5.2	91	156.0	8.7	6.1	2.61
461	01:20:17	−73:09:39	6.4	111	147.7	7.1	9.2	2.51
462	01:20:19	−72:56:04	2.2	38	144.9	3.3	6.9	0.58
463	01:20:19	−73:44:14	13.1	229	140.2	13.4	10.0	3.98
464	01:20:29	−72:52:57	3.8	67	172.2	7.6	5.2	2.17
465	01:20:45	−72:39:14	12.5	218	151.3	19.7	6.5	4.43
466	01:20:48	−74:40:57	5.3	93	183.9	4.6	11.9	1.80
467	01:21:01	−72:49:40	1.0	17	139.8	1.1	9.0	−1.54
468	01:21:19	−73:48:15	13.3	233	160.4	18.5	7.4	4.41
469	01:21:30	−72:00:58	11.0	191	197.7	13.1	8.6	3.79
470	01:21:34	−75:08:59	19.0	332	168.7	21.1	9.2	4.89
471	01:21:37	−73:30:02	2.9	51	149.7	3.4	8.8	0.86
472	01:21:40	−73:17:58	6.1	106	173.4	9.9	6.3	2.91
473	01:21:45	−71:21:19	1.5	25	206.6	2.9	5.1	0.08
474	01:22:17	−73:25:11	2.7	47	182.3	3.0	9.0	0.66
475	01:22:39	−71:43:36	14.0	245	188.4	14.7:	9.8	4.15
476	01:22:46	−71:54:10	4.1	71	189.3	12.0	3.5	2.81
477	01:22:49	−73:14:20	2.9	50	145.5	4.2	7.1	1.14
478	01:22:58	−73:23:18	2.0	35	160.1	3.0	6.7	0.41
479	01:22:59	−72:59:09	6.1	106	164.9	14.1	4.4	3.37
480	01:23:00	−73:05:11	3.8	67	149.6	5.1	7.7	1.64
481	01:23:05	−73:21:44	8.5	148	142.1	13.4	6.5	3.59
482	01:23:26	−73:07:58	2.9	51	139.0	4.2	7.1	1.15
483	01:24:25	−72:25:02	7.3	127	146.8	28.0	2.7	4.43
484	01:24:27	−72:29:33	11.1	194	193.6	15.1	7.6	3.98
485	01:24:30	−72:17:23	16.7	291	177.0	24.7	6.9	4.98
486	01:24:32	−74:39:05	3.3	58	188.3	7.1	4.8	1.96
487	01:24:34	−71:22:36	10.2	179	205.6	10.9:	9.6	3.49
488	01:24:39	−73:13:18	9.0	156	157.8	14.1	6.5	3.71
489	01:25:42	−72:12:05	12.5	218	171.1	32.3	4.0	5.07
490	01:25:46	−73:06:35	4.2	74	183.2	8.0	5.4	2.31
491	01:25:52	−74:11:20	27.6	482	175.1	31.8:	8.9	5.75
492	01:26:30	−71:28:55	4.2	74	195.8	5.9	7.4	1.92
493	01:26:32	−71:53:17	14.5	253	205.2	9.6:	15.4	3.63
494	01:26:56	−72:49:12	6.3	110	176.0	20.7	3.1	3.90
495	01:27:47	−73:02:16	10.2	179	158.0	17.6	6.0	4.11
496	01:28:36	−72:46:34	3.8	67	156.8	5.1	7.7	1.65

Table 1 – *continued*

SMC H I Shell	RA	DEC	Shell Radius ($'$)	r_s (pc)	Heliocentric Velocity V (km s^{-1})	Expansion Velocity v_s (km s^{-1})	Age T_s (10^6yr)	Wind Luminosity $\log(L_s/n_0)$ ($L_\odot$ cm^3)
	(J2000)							
497	01:28:50	−73:25:47	11.1	194	180.3	13.4	8.5	3.83
498	01:29:01	−73:15:04	11.8	207	173.1	8.0	15.2	3.21
499	01:30:25	−73:27:44	10.2	179	160.7	14.2	7.4	3.84
500	01:30:33	−73:36:42	13.3	233	163.0	15.4	8.8	4.17
501	01:31:59	−73:28:08	2.7	47	185.8	6.9	4.0	1.72

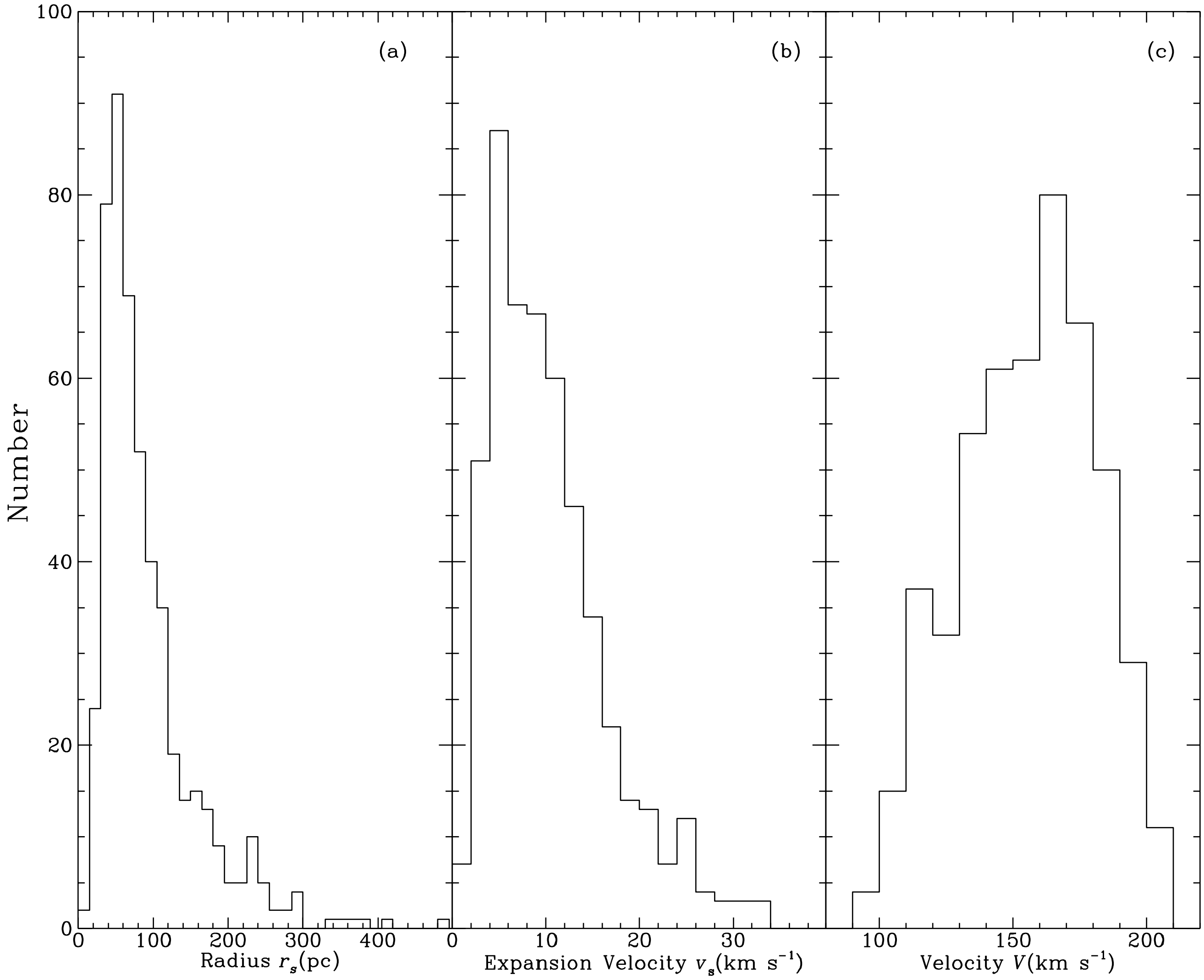

Figure 7. The distribution of (a) radii, (b) expansion velocities, and (c) heliocentric velocities for the 501 SMC shells and supershells.

though there may be some confusion with SMC HI-495 and 499. The derived age of SMC HI-498 is 1.5×10^7 yr, which makes it one of the older shells in Table 1. The radius of 207 pc is lower than Meaburn's value of 300 pc. Spectroscopic confirmation of this identification is required.

In general, our shell catalogue is insensitive to very large shells, very small shells, and shells in complex regions. Large shells may fall below our column density limit, or may be too diffuse for the interferometer to detect, or may simply be too vulnerable to disruption in the complex environment of the SMC.

5.1 Kinematics of the shells

The central heliocentric velocities of the 501 shells presented in Table 1 are assumed to correspond to the heliocentric radial velocities of the central star cluster. Thus they con-

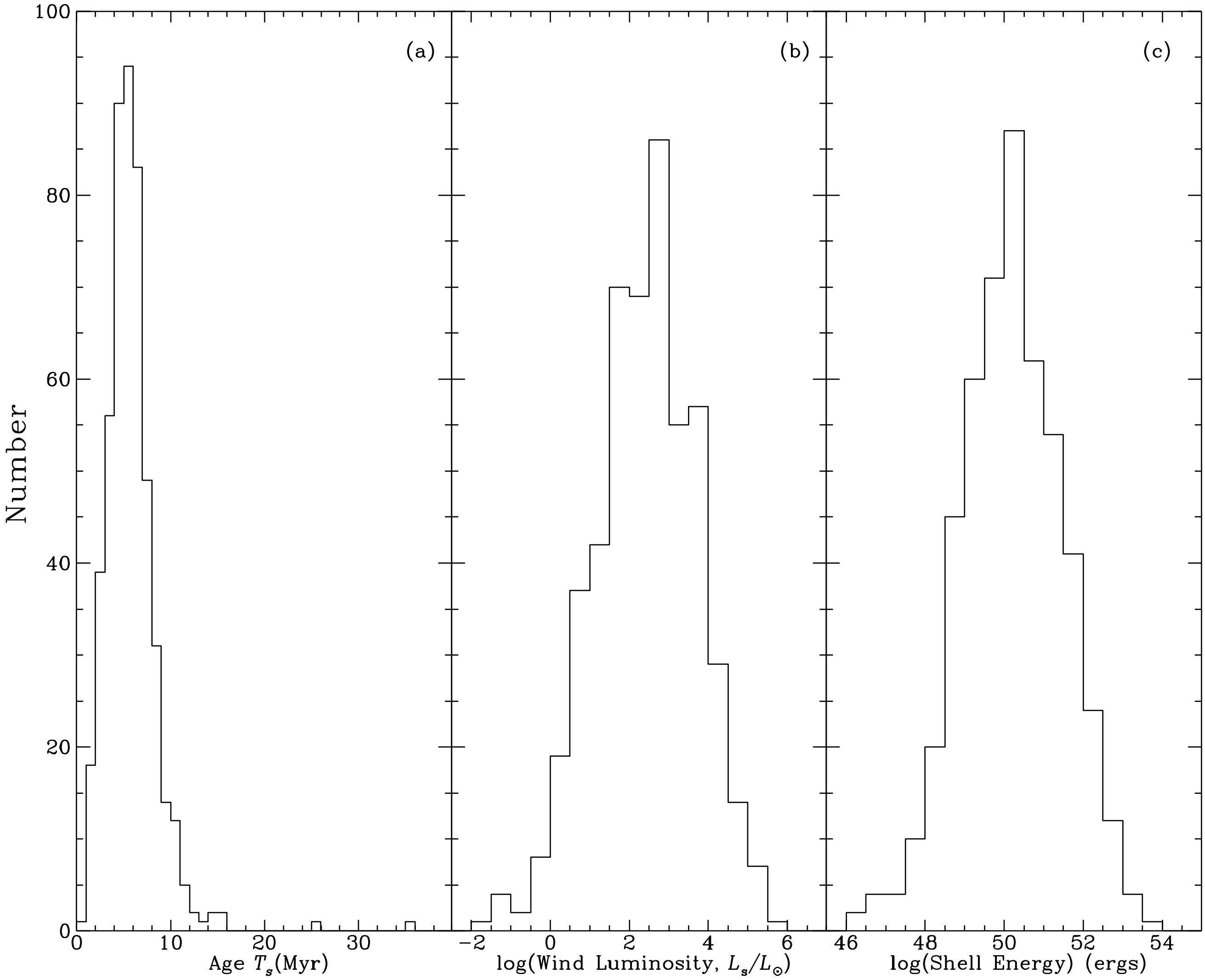

Figure 8. The distribution of (a) age, (b) wind luminosity, and (c) total wind energy of the SMC shells and supershells. The wind luminosity and energy assume a density $n_o = 1$ cm^{-3}.

stitute the largest existing homogeneous sample of young objects in the SMC with well-determined velocities. The objects are evenly distributed over the main body and the Wing of the SMC. Moreover, the statistical errors of the velocities are comparatively low, ranging from 1 – 5 km s^{-1}, with most being < 3 km s^{-1}. Given the large size of the sample, its homogeneity, its spatial distribution and the small statistical errors of the velocities, it is well worth investigating its kinematical characteristics and comparing them with those of other populations in the SMC.

The velocity histogram of Fig. 7c is in itself very instructive: there is no evidence of bimodality in the velocity distribution. This agrees with the study of Maurice et al. (1987), who obtained radial velocities (with similar errors of the individual velocities to the present) for 255 supergiants in the main body and Wing of the SMC. They also did not find a double-peaked structure in the velocity histogram (though they mention that the subset of OBA stars in their sample might show such a structure). Both the present study and that of Maurice et al. contradict earlier results (see Torres & Carranza 1987 for a review) which suggest the presence of two or more distinct radial velocity groups among young populations in the SMC. The velocity separation between these groups was supposed to be about 30 km s^{-1}, which is clearly large enough to be detectable in the present study. It is possible that such bimodality may appear in particular directions (or in small samples resulting from poor statistics), given the great complexity of the SMC kinematics, especially of young stars and gas.

The range of radial velocities in the present sample is 97 – 208 km s^{-1}. No higher velocity objects, which have been found in other samples of stars (e.g. Hatzidimitriou, Cannon & Hawkins 1993; Hatzidimitriou et al. 1997) are present, implying that such objects are probably no longer inside the main gaseous body of the SMC. There is an overall tendency for high-velocity objects to be concentrated in the north-east with the lower velocity ones concentrated in the south-west, as is also immediately obvious on the isovelocity images. Much of this trend may due to parallax, combined with the expected large proper motion of the SMC, as is the case for the LMC (Jones, Klemola & Lin 1994).

The unweighted mean heliocentric velocity of the present sample is 155.3 ± 1.1 km s^{-1}, and the unweighted velocity dispersion is 25.0 ± 0.6 km s^{-1}. Including only the 43 objects belonging to the Wing region ($\alpha > 01^{\rm h}20^{\rm m}$), we get a higher mean heliocentric velocity (as expected) of 170 ± 3 km s^{-1}, and a lower velocity dispersion of 19.4 ± 1.5 km s^{-1}.

Table 2 summarizes results from earlier studies, both for young and old objects in the SMC. This list is by no means comprehensive. It includes mostly relatively recent studies of samples that are distributed over the entire 'main body' and Wing region of the SMC. Generally the mean velocities (heliocentric in all cases) agree reasonably well, allowing for small zero-point errors that may be present in the different studies. The velocity dispersions are also comparable both for young and old objects, with the exception of the supergiants studied by Maurice et al. (1987) which show a significantly lower value. The quoted velocity dispersions are affected by rotation, streaming motions, expansion, and tidal interaction with the LMC and the Galaxy (e.g. Hatzidimitriou et al. 1993), and so are not immediately useful for calculating total mass. A more detailed analysis of the kinematics of the H I will follow in a subsequent paper.

6 THE STRUCTURE AND EVOLUTION OF THE SMC

The shell expansion velocities v_s (Fig. 7b) are typically a significant fraction of the SMC escape velocity $v_{\rm esc} \approx 50$ km s^{-1}, implying that the SMC is suffering severe disruption by the continuing burst of star formation. The catalogued shells are driven by a total wind luminosity $\Sigma L_s = 3.6 \times 10^6 L_\odot$ for $n_\circ = 1$ cm^{-3}, giving a time-integrated energy of 2.9×10^{54} erg. With no radiative cooling, 6/11 of this goes into PdV work on the shell, with the remainder appearing as interior thermal energy (Shull & Saken 1995). The available energy is therefore a significant fraction (~ 5 per cent) of the H I+He gravitational binding energy of $\sim 3 \times 10^{55}$ erg (assuming $M_{\rm H+He} = 6 \times 10^8 M_\odot$, radius = 2 kpc, and H+He gas fraction = 0.5). For the smaller shells, radiative cooling will remove much of this energy once the shell has been stalled by the ambient ISM pressure. However, most of the shell kinetic energy is contained in the supershells, which are very likely to break out from the main gaseous body of the SMC.

Such disruption argues against a tilted disk-like structure for the SMC – the line-of-sight depth for the H I is likely to be as great as its projection on the sky (~ 4 kpc). This agrees with Cepheid results which imply depths of 4 kpc (Caldwell & Coulson 1986; Welch et al. 1987), or even greater (Hatzidimitriou & Hawkins 1989; Mathewson et al. 1988). The total volume occupied by the catalogued shells is 5.3 kpc^3. If an H I radius of 2 kpc is assumed, then the volume fraction of the SMC occupied by the catalogued shells (assuming minimum overlap) is ~ 0.2. In three dimensions, this would give the SMC a 'Swiss cheese' morphology. However, the H I structure in many parts of the SMC is so complex (Figs 4, 5 & 9) that shell identification is precluded, and the filling factor probably greatly exceeds this. We therefore propose that the SMC has a bubbly or frothy appearance in three dimensions.

We now turn to the age distribution for the shells which, except for a small population of slightly older shells (~ 8 Myr) in the south, appear to have a uniform dynamical age of about 5.4 Myr and an intrinsic age dispersion of about 2 Myr. This implies an exceptional degree of coherence in the star-formation activity throughout the SMC. Such coherence is a puzzle even for the theory of stochastic self-propagating star-formation (Gerola, Seiden & Schulman 1980), where one burst of star-formation gives rise to a shock which propagates into the ISM, sweeps up gas and leads to fragmentation and collapse into new regions of star formation (Elmegreen 1989). This is because the mean shell age is much smaller than the crossing time of a typical shock, ~ 20 Myr for a 100 km s^{-1} shock wave. This theory otherwise seems the natural explanation for structure formation in the SMC, where several examples of the phenomenon can be seen. For example: (1) Fig. 6 shows small shells forming on the rims of primary shells; (2) the HII region N90 or DEM S166 (Henize 1956; Davies, Elliott & Meaburn 1976) lies close to the rim of Meaburn supershell SMC 1 or DEM S167 (Meaburn 1980) and SMC HI-498. The optical velocity for N90 of 176.6 km s^{-1} (Smith & Weedman 1973) is close to the central velocity of 173.1 km s^{-1} for SMC HI-498.

There is no strong observational selection effect that makes us preferentially sensitive to shells of age ~ 5 Myr. We note that, in contrast to the present results, a study of 51 H I shells in Holmberg II, a galaxy with a similar mass and gas fraction, found a much larger fractional age spread, a much greater mean age (61 Myr), and found no shells younger than 9 Myr (Puche et al. 1992). However, we do note that 5 Myr is the time taken by the most massive stars to evolve off the main sequence, and is the age at which, for a coeval star cluster, the ratio of Wolf-Rayet to O stars is the highest (Shull & Saken 1995). For a cluster of 100 OB stars, Shull & Saken show that the wind luminosity of Wolf-Rayet stars in the age range $4 \sim 8$ Myr, is approximately equal to both the stellar wind luminosity and the supernova energy deposition rates. This extra luminosity re-accelerates the shell and can cause the dynamical age to underestimate the true age by ~ 40 per cent for a coeval star cluster in this interval. In Shull & Saken's 'class 4' model, which has a constant initial mass function but is non-coeval, the dynamical age can underestimate the true age by up to a factor of ~ 3.

For the smaller shells, for which the supernova energy deposition rate can no longer be taken to be constant, re-acceleration may occur in a similar way in cases where the supernova energy is not all thermalized (Tenorio-Tagle et al. 1990; Oey 1996). This acceleration can again cause the true shell age to be underestimated very significantly. A possible example of this is DEM L152 in the LMC, where the dynamical time-scale ${}^3/_5(r_s/v_s) = 5 \times 10^5$ yr for the Hα superbubble is much less than the true age of $\gtrsim 10$ Myr suggested by the H-R diagram for the interior stars of the OB association LH 47/48 (Oey & Massey 1995).

Such effects may diminish the age-coherence problem. However, there is still the problem of having a large number of young shells. We attribute this to a large-scale event in the recent history of the SMC. The previous encounter between the SMC and LMC, as modelled by Murai & Fuji-

Table 2. Mean heliocentric radial velocity $< V >$, and velocity dispersion $\sigma(V)$, of the H I shells in the SMC compared with other young and old populations.

Study	Type	Sample size	$< V >$ (km s^{-1})	$\sigma(V)$
		Young Populations		
Maurice et al. (1987)	Supergiants	255	162 ± 1	18
Mathewson et al. (1988)	Cepheids	61	149 ± 3	22 ± 3
This paper	H I shells	501	155 ± 1	25 ± 1
		Intermediate Age and Old Populations		
Dopita et al. (1985)	Planetary Nebulae	44	146 ± 4	25 ± 3
Hardy, Suntzeff & Azzopardi (1989)	Carbon Stars	131	148 ± 2	27 ± 2
Hatzidimitriou et al. (1997)	Carbon Stars[a]	72	149 ± 3	26 ± 2

[a] This sample is not located in the main body of the SMC but in the outer regions and Wing.

moto (1980), is likely to have happened 200 Myr ago, which is beyond the time-scale of interest here. However, the SMC is currently close to perigalacticon (Gardiner et al. 1994), and so a collisional or tidal event associated with this is a possibility.

The ultimate fate of the remaining SMC H I gas may depend on the existence of a dark halo to the SMC. Without a dark halo, and with a Galaxy-to-SMC mass ratio of 300, the tidal radius of the SMC is ~ 7 kpc. This is unlikely to be sufficient to prevent slow disintegration in the Galactic tidal field, unless the SMC possesses a dark halo. At the present rate of energy deposition, it will take only ~ 100 Myr for the mechanical wind energy to exceed the binding energy of all the neutral gas in the SMC (longer if the dynamical ages are significantly underestimated). Similarly, the next close encounter with the LMC could cost the SMC a large fraction of its current neutral gas, and turn the Magellanic Stream into a river. More information on the previous encounter between the LMC and SMC would be useful in this regard, for example from high-resolution H I images of the bridge region.

7 THE DEPTH OF THE SMC

In the literature, the SMC was often regarded as consisting of several distinct components (e.g. McGee & Newton 1981; Martin, Maurice & Lequeux 1989). Mathewson and coworkers have suggested the existence of a spatially distinct 'mini-Magellanic Cloud' lying behind the SMC with a velocity separation of +30-40 km s^{-1} (Mathewson & Ford 1984; Mathewson, Ford & Visvanathan 1986; Mathewson et al. 1987). This suggestion is based on H I line-splitting and on observations of Cepheid variables which indicate that the distance of this cloud behind the SMC is between 6 and 17 kpc. Somewhat smaller depths have been measured by other authors (Caldwell & Coulson 1986; Welch et al. 1987).

However, the new results show that most, if not all, of the line-splitting apparent in previous SMC H I data appears to be caused by shells and supershells (a view originally expressed by Hindman 1967, but later rejected by Mathewson & Ford 1984). In many parts of the SMC, the line-splitting arises from single shells. Therefore, the line-of-sight separation of the two velocity components will not exceed the measured shell diameters, which range up to 1.1 kpc. Moreover, given that the age of most of the shells is likely to be shorter than the time taken for Cepheid progenitors to evolve off the main-sequence (e.g. Becker 1985), it is unlikely that any of the SMC Cepheid population is directly associated with any of the shells. Depth measurements using Cepheids are measuring an older Population I component.

In Fig. 9, we show a series of position-velocity slices along the apparent kinematic major axis of the SMC. Slice (c) is the approximate major axis. The other slices are parallel and are separated, along the minor axis, by 1.5 arcmin. This region is similar to the 'major axis' slice (Fig. 9) examined by Mathewson & Ford (1984). and shows that, although this region is very complex, much of the structure is resolved into shells/holes. For example, in the south-west at a major-axis offset of $-2\overset{\circ}{.}4$, SMC HI-10 is very prominent ($r_s = 409$ pc, $v_s = 19.6$ km s^{-1}). In the north-east at major-axis offset $0\overset{\circ}{.}0$, there is a group of shells of which SMC HI-300 ($r_s = 274$ pc, $v_s = 27.7$ km s^{-1}) is the most prominent. In the central part of Fig. 9 ($\alpha = 00^{\rm h}53^{\rm m}, \delta = -72^\circ 36'$, J2000), there is more complex line splitting, and individual shells are harder to discern. In this region, the central shell velocities range from 120 to 180 km s^{-1}. The distance spread of the shells in this region is not directly constrained, so there is room for some intrinsic distance spread. However, in cases where secondary shell formation is responsible, the distance spread will be moderate.

8 SUMMARY

We have presented images from an H I aperture synthesis mosaic of the SMC, and presented a catalogue of 501 H I shells and supershells. This data set is of considerable value in understanding the nature of the interstellar medium in one of the closest gas-rich galaxies to us. The main conclusions of the present study are that the SMC cannot be modelled as a simple tilted disk. Because of the combined effects of stellar winds and supernovae, the SMC is probably destined for breakup, unless it has a massive halo. The next close encounter with the LMC will liberate a substantial part of the gaseous and stellar content of the SMC. The reason for the large amount of mechanical energy is a very young and coherent burst of star formation across the face of the

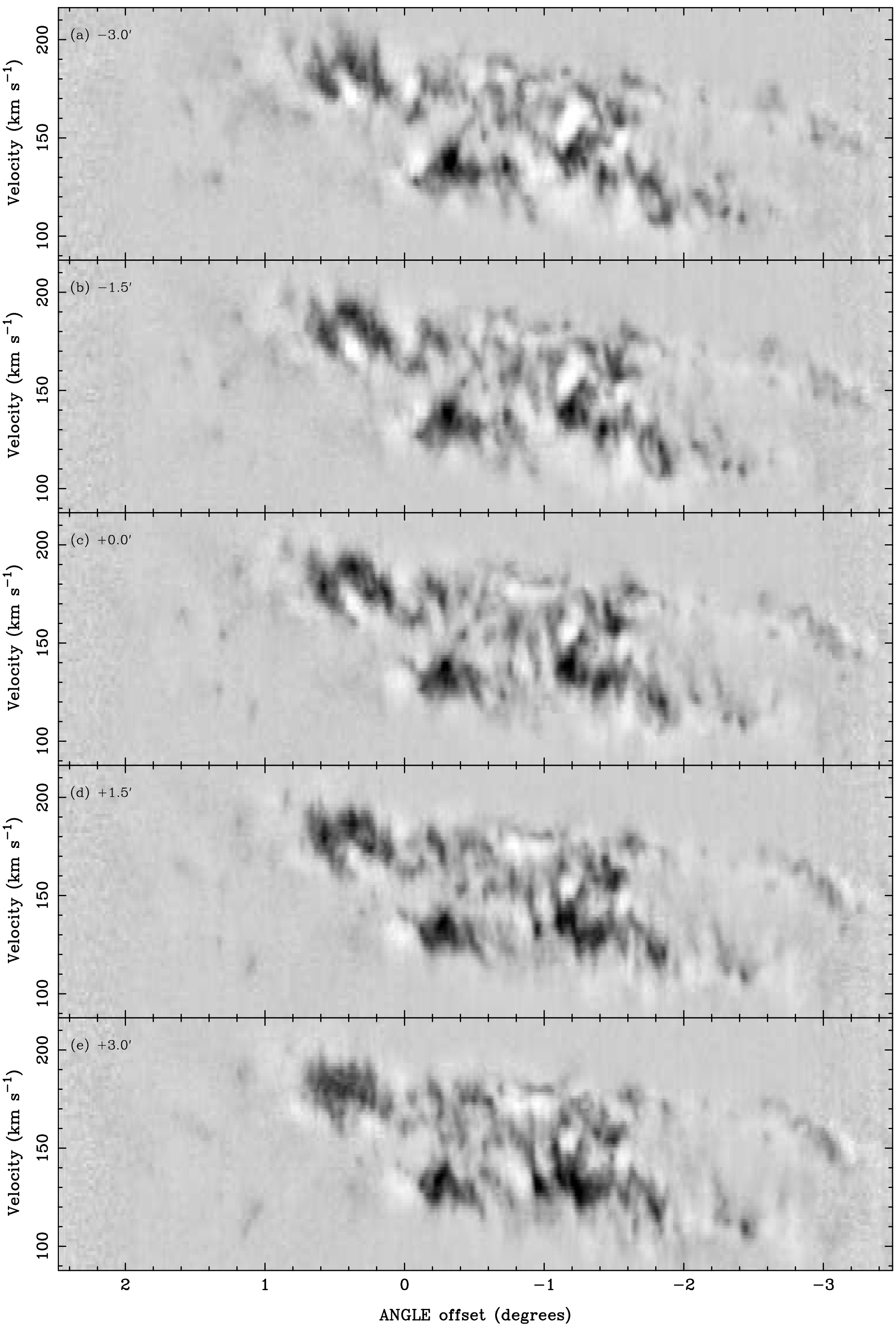

Figure 9. Position-velocity images parallel to the apparent kinematic major axis of the SMC (see also figure 4 of Mathewson & Ford 1984), defined here as being along a line of pa 47° which passes through the (arbitrary) reference point RA $01^{\rm h}00^{\rm m}50^{\rm s}$, Dec $-72°21'37''$ (J2000). The $x-$axis is the offset from the reference point along the major axis (positive offsets being towards the north-east). For each parallel slice, the offset normal to the major axis is indicated, and ranges from -3 to $+3$ arcmin (the negative offsets being towards the south-east). Many shells and supershells can be seen, with the largest being SMC HI-10 in the south-west (angle offset $\sim -2\overset{\circ}{.}4$). The grey-scale range is -17 to 87 K (linear transfer function).

SMC. The mean age is 5.4 Myr, estimated from the dynamics of the H I shells, although this may be an underestimate depending on cluster-evolution details. The intrinsic dispersion in shell ages is only 2 Myr, and the southern part of the SMC appears to have a mean age which is greater by 2.5 Myr. We believe that some previous studies of the SMC have wrongly interpreted multiple velocity components as separate structures in real space whereas we find, on the whole, that these components are the result of the combined effect of the numerous expanding shells and supershells which are seen for the first time in H I at high resolution.

Our future studies of the SMC will include single-dish data, so that total column densities can be measured. This will allow the study of the largest supershells to which the present study is insensitive. The data in the form of a FITS cube are available from the authors on request (there is a nominal media charge). Table 1 is available via anonymous ftp://ftp.atnf.csiro.au/pub/data/smc, or on request.

ACKNOWLEDGMENTS

We thank Neil Killeen for converting CGDISP to accept non-linear coordinates, Richard Gooch and Tom Oosterloo for help with data cube visualization, Sally Oey for helpful comments, and Sungeun Kim and Mike Bessell for permission to reproduce the 2-inch Hα image in advance of publication.

REFERENCES

Becker S.A., 1985, in B.F. Madore ed., Proc. IAU Colloq. 82, Cepheids: Theory and Observations. Cambridge University Press, Cambridge, p.104
Brinks E., Bajaja E., 1986, A&A, 169, 14
Brück M.T., 1980, A&A, 87, 92
Caldwell J.A.R., Coulson I.M., 1986, MNRAS, 218, 223
Chu Y.-H., Chang H-W., Su Y-L., Mac Low M.-M., 1995, ApJ, 450, 157
Cornwell T.J., 1988, A&A, 202, 316
Cornwell T.J., Holdaway M.A., Uson J.M., 1993, A&A, 271, 697
Crovisier J., Dickey J.M., 1983, A&A, 122, 282
Davies R.D., Elliott K.H., Meaburn J., 1976, MmRAS, 81, 89
Dopita M.A., Ford H.C., Lawrence C.J., Webster B.L., 1985, ApJ, 296, 390
Ekers R.D., Rots A.H., 1979, in C. van Schooneveld, ed., Proc. IAU Colloq. 49, Image Formation from Coherence Functions in Astronomy. Reidel, Dordrecht, p.61
Elmegreen B.G., 1989, ApJ, 344, 306
Gardiner L.T., Sawa T., Fujimoto M., 1994, MNRAS, 266, 567
Gerola H., Seiden P.E., Schulman L.S., 1980, ApJ, 242, 517
Goudis G., Meaburn J., 1978, A&A, 68, 189
Hardy E., Suntzeff N.B., Azzopardi M., 1989, ApJ, 344, 210
Hatzidimitriou D., Hawkins M.R.S., 1989, MNRAS, 241, 667
Hatzidimitriou D., Cannon R.D., Hawkins M.R.S., 1993, MNRAS, 261, 873
Hatzidimitriou D., Croke B.F., Morgan D.H., Cannon R.D., 1997, A&AS 122, 507
Heiles C., 1979, ApJ, 229, 533
Henize K.G., 1956, ApJS, 2, 315
Hindman J.V., 1967, Australian J. Phys., 20, 147
Irwin M.J., 1991, in Haynes, R.F., Milne, D.K., eds, Proc. IAU Symp. 148, The Magellanic Clouds. Kluwer, Dordrecht, p.453
Jones B.F., Klemola A.R., Lin D.N.C., 1994, AJ, 107, 1333
Kendall M.G., Stuart A., 1963, The Advanced Theory of Statistics, Volume 1. Charles Griffin, London
McCray R., Kafatos M., 1987, ApJ, 317, 190
McGee R.X., Newton L.M., 1981, Proc. Astr. Soc. Australia, 4, 189
Martin N., Maurice E., Lequeux J., 1989, A&A, 215, 219
Martimbeau N., Carignan C., Roy J.-R., 1994, AJ, 107, 543
Mathewson D.S., Ford V.L., 1984, in van den Bergh, S., de Boer, K.S., eds, Proc. IAU Symp. 108, Structure and Evolution of the Magellanic Clouds. Reidel, Dordrecht, p.125
Mathewson D.S., Ford V.L., Visvanathan N., 1986, ApJ, 301, 664
Mathewson D.S., Wayte S.R., Ford V.L., Ruan, K., 1987, Proc. Astr. Soc. Australia, 7, 19
Mathewson D.S., Ford V.L., Visvanathan N., 1988, ApJ, 333, 617
Maurice E. et al., 1987, A&AS, 67, 423
Meaburn J., 1980, MNRAS, 192, 365
Murai T., Fujimoto M., 1980, PASJ, 32, 581
Oey M.S., 1996, ApJ, 467, 666
Oey M.S., Massey P., 1995, ApJ, 452, 210
Puche D., Westpfahl D., Brinks E., Roy J.-R., 1992, AJ, 103, 1841
Rubio M. et al., 1993, A&A, 271, 1
Ryder S.D., Staveley-Smith L., Malin D., Walsh W., 1995, AJ, 109, 1592
Sault R.J., Teuben P.J., Wright M.C.H., 1995, in Shaw R.A., Payne H.E., Hayes J.J.E., eds, Astronomical Data Analysis Software and Systems IV, ASP Conf. Series, vol. 77. Astronomical Society of the Pacific, San Francisco, p.433
Sault R.J., Staveley-Smith L., Brouw W.N., 1996, A&AS 120, 375
Schwering P.B.W., Israel F.P., 1990, Atlas and Catalogue of Infrared Sources in the Magellanic Clouds. Kluwer, Dordrecht
Shull M.J., Saken J.M., 1995, ApJ, 444, 663
Smith M.G., Weedman D.W., 1973, ApJ, 179, 461
Staveley-Smith L., Sault R.J., McConnell D., Kesteven M.J., Hatzidimitriou D., Freeman K.C., Dopita M.A., 1995, Publ. Astr. Soc. Australia, 12, 13
Tenorio-Tagle G., Bodenheimer P., 1988, ARA&A, 26, 145
Tenorio-Tagle G., Bodenheimer P., Franco J., Różyczka M., 1990, MNRAS, 244, 563
Torres G., Carranza G.J., 1987, MNRAS, 226, 513
Weaver R., McCray R., Castor J., Shapiro P., Moore R. 1977, ApJ, 218, 377
Welch D.L., McLaren R.A., Madore B.F., McAlary C.W. 1987, ApJ, 321, 162

APPENDIX A: COORDINATES

The data in this paper and in the FITS cubes available are presented in North Celestial Pole (NCP) projection. The relationship between pixel coordinates (x, y) in radians and RA, Dec (α, δ) (J2000) in radians is defined as follows:

$$\alpha = \alpha_\circ + \tan^{-1}\left(\frac{\Delta x}{\cos\delta_\circ - \Delta y \sin\delta_\circ}\right) \tag{A1}$$

$$\delta = \frac{\delta_\circ}{|\delta_\circ|}\cos^{-1}\left(\frac{\cos\delta_\circ - \Delta y\sin\delta_\circ}{\cos(\alpha-\alpha_\circ)}\right), \tag{A2}$$

where $\Delta x = (x - x_\circ)dx$, $\Delta y = (y - y_\circ)dy$, $\alpha_\circ = 00^{\rm h}55^{\rm m}$ (J2000), and $\delta_\circ = -72°50'$ (J2000). The reference point which corresponds to $(\alpha_\circ, \delta_\circ)$ is given by $(x_\circ, y_\circ) = (342.0, 321.0)$ in the full-size distributed images. The pixel size is $dx = dy = 30''$.